Cell Metabolism

Article

Foxp3 confers long-term efficacy of chimeric antigen receptor-T cells via metabolic reprogramming

Graphical abstract

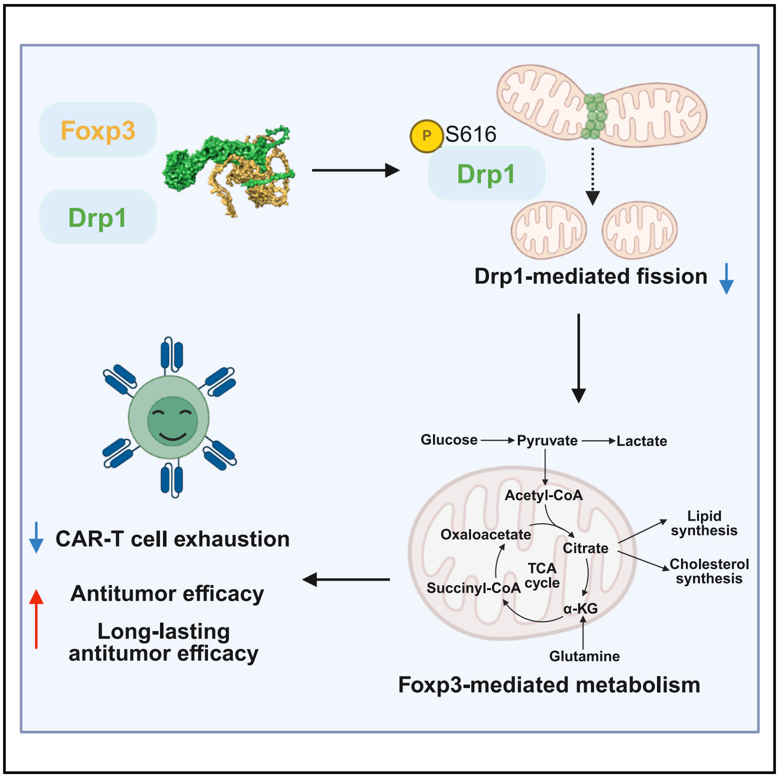

Authors

Congyi Niu, Huan Wei,
Xuanxuan Pan, ..., Jie Liu, Yiwei Chu,
Feifei Luo

Correspondence

yiweichu@fudan.edu.cn (Y.C.),
feifeiluo@fudan.edu.cn (F.L.)

In brief

Niu et al. report that engineering CAR-T cells with Treg transcription factor Foxp3 confers tumor microenvironment-resilient metabolic adaptations while avoiding Treg-like immunosuppression. These metabolic alterations enable CAR-T cells to exhibit sustained antitumor potency with attenuated exhaustion phenotypes, offering a therapeutic strategy to enhance CAR-T cell efficacy through metabolic adaptation engineering.

Highlights

- CAR-T$_{Foxp3}$ cells exhibit distinct metabolic reprogramming from CAR-T$_{Conv}$ cells
- Foxp3's interaction with Drp1 drives this metabolic shift of CAR-T$_{Foxp3}$ cells
- CAR-T$_{Foxp3}$ cells do not acquire regulatory T cell-like immunosuppression
- CAR-T$_{Foxp3}$ cells show reduced exhaustion and enhanced antitumor efficacy

Niu et al., 2025, Cell Metabolism *37*, 1426–1441
June 3, 2025
https://doi.org/10.1016/j.cmet.2025.04.008

CellPress
OPEN ACCESS

Cell Metabolism

Article

Foxp3 confers long-term efficacy of chimeric antigen receptor-T cells via metabolic reprogramming

Congyi Niu,[1,2] Huan Wei,[1] Xuanxuan Pan,[2] Yuedi Wang,[1,3] Huan Song,[2] Congwen Li,[1] Jingbo Qie,[1] Jiawen Qian,[1] Shaocong Mo,[2] Wanwei Zheng,[2] Kameina Zhuma,[1] Zixin Lv,[1] Yiyuan Gao,[1] Dan Zhang,[1] Hui Yang,[1] Ronghua Liu,[1] Luman Wang,[1] Wenwei Tu,[4] Jie Liu,[1,2] Yiwei Chu,[1,3,*] and Feifei Luo[1,2,5,*]

[1]Department of Immunology, School of Basic Medical Sciences, Biotherapy Research Center and Institutes of Biomedical Sciences, Fudan University, Shanghai 200032, China
[2]Department of Digestive Diseases, Huashan Hospital, Fudan University, Shanghai 200040, China
[3]Shenzhen Institute of Synthetic Biology, Shenzhen Institutes of Advanced Technology, Chinese Academy of Sciences, Shenzhen 518055, China
[4]Department of Paediatrics & Adolescent Medicine, School of Clinical Medicine, LKS Faculty of Medicine, The University of Hong Kong, Hong Kong SAR, China
[5]Lead contact
*Correspondence: yiweichu@fudan.edu.cn (Y.C.), feifeiluo@fudan.edu.cn (F.L.)
https://doi.org/10.1016/j.cmet.2025.04.008

SUMMARY

The tumor microenvironment, characterized by low oxygen tension and scarce nutrients, impairs chimeric antigen receptor (CAR)-T cell metabolism, leading to T cell exhaustion and dysfunction. Notably, Foxp3 confers a metabolic advantage to regulatory T cells under such restrictive conditions. Exploiting this property, we generated CAR-T_{Foxp3} cells by co-expressing Foxp3 with a third-generation CAR construct. The CAR-T_{Foxp3} cells exhibited distinct metabolic reprogramming, marked by downregulated aerobic glycolysis and oxidative phosphorylation coupled with upregulated lipid metabolism. This metabolic shift was driven by Foxp3's interaction with dynamin-related protein 1. Crucially, CAR-T_{Foxp3} cells did not acquire regulatory T cell immunosuppressive functions but instead demonstrated enhanced antitumor potency and reduced expression of exhaustion markers via Foxp3-mediated adaptation. The potent antitumor effect and absence of immunosuppression were confirmed in a humanized immune system mouse model. Our findings establish a metabolic reprogramming-based strategy to enhance CAR-T cell adaptability within the hostile tumor microenvironment while preserving therapeutic efficacy.

INTRODUCTION

Chimeric antigen receptor (CAR)-T immunotherapy is effective against hematological cancers.[1–3] However, its effectiveness in solid tumors is low, and responses are transient.[4,5] CAR-T cells are always malnourished in the tumor microenvironment (TME) and are stimulated continually by tumor antigens, resulting in their exhaustion and ATP synthesis deficiency.[6,7] This is considered one of the major bottlenecks in CAR-T immunotherapy for solid malignancies.

Physiologically, the metabolism of distinct T cell subpopulations differs, and T cells switch their metabolic pathways during differentiation. Naive T (Tn) lymphocytes remain quiescent and rely on oxidative phosphorylation (OXPHOS) to maintain survival.[8,9] After antigen stimulation, Tn cells differentiate into effector T cells (Teffs) and shift their metabolic strategy from OXPHOS to aerobic glycolysis, which enables them to perform effector functions.[10,11] As a subpopulation of T cells, regulatory T cells (Tregs) exhibit a metabolism distinct from that of Teffs, characterized by elevated lipid metabolism and diminished aerobic glycolysis and OXPHOS.[12–15] Tregs are less susceptible to glycolysis,[16–18] and genetic deletion of the glucose transporter Glut1 does not have any effect on Tregs but inhibits $CD4^+$ T cell differentiation.[16] The low OXPHOS in Tregs is attributed to decreased mTORC2 activity,[14] and upregulation of OXPHOS during Treg polarization by α-ketoglutarate diminishes the differentiation of Tn cells to Tregs substantially.[15] Increasing evidence suggests that distinctive metabolic patterns of Tregs cause their long-term survival and potent expansion in the hypoxic and acidic TME created by highly proliferating cancer cells.[19–22] Moreover, recent studies have highlighted Foxp3 as a key regulator of Treg metabolism.[14,23,24] However, it remains unclear whether Foxp3 can be overexpressed in Teffs, especially in CAR-T cells, to alter their metabolic characteristics and enable long-term survival and function in TME.

To evaluate this aspect, in this study, CAR-T_{Foxp3} cells were constructed by co-expressing Foxp3 with third-generation

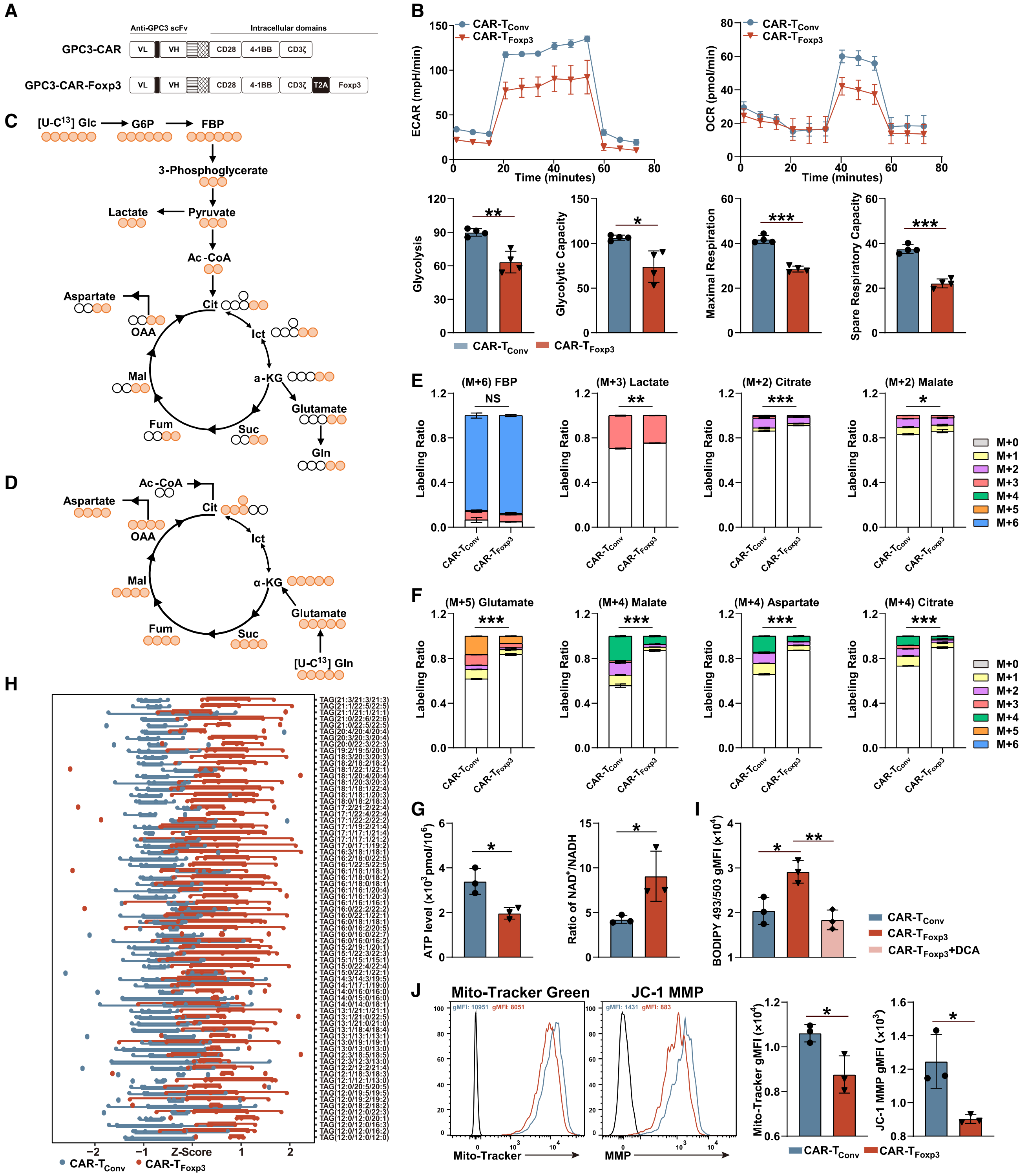

Figure 1. CAR-T$_{Foxp3}$ cells acquire distinct metabolic characteristics from CAR-T$_{Conv}$ cells

(A) Schematic diagram of third-generation GPC3-CARs.

(B) ECAR and OCR of different CAR-T cells and quantification of glycolysis, glycolytic capacity, maximal respiration, and spare respiratory capacity (*n* = 4 biological replicates). Representative results from two independent experiments.

(C and D) Schematic representations of metabolic flux from [U-C13]-glucose and [U-C13]-glutamine. The white circle represented the C12 atom, and the orange circle represented the radiolabeled C13 atom. During the cellular metabolism of [U-C13]-glucose and [U-C13]-glutamine, unique labeling patterns in the

(legend continued on next page)

CAR to reprogram CAR-T cell metabolism. We explored the cytotoxicity and persistence and excluded the immunosuppression of CAR-T$_{\text{Foxp3}}$ cells *in vitro* and *in vivo*. The data could facilitate the development of metabolic reprogramming-based strategies for improving CAR-T cell immunotherapy.

RESULTS

CAR-T$_{\text{Foxp3}}$ cells acquire distinct metabolic characteristics from CAR-T$_{\text{Conv}}$ cells

We first investigated whether Foxp3 overexpression could alter CAR-T cell metabolism. Given the superior expansion and persistence of the third-generation CAR compared with its second-generation counterpart,[25] we utilized the third-generation CAR. We activated human T lymphocytes from healthy donors and infected them with GPC3-CAR to generate conventional GPC3-CAR-T (CAR-T$_{\text{Conv}}$) cells or with GPC3-CAR plus Foxp3 to develop GPC3-CAR-T$_{\text{Foxp3}}$ (CAR-T$_{\text{Foxp3}}$) cells (Figures 1A and S1A). We measured metabolic parameters such as the extracellular acidification rate (ECAR) and oxygen consumption rate (OCR), and CAR-T$_{\text{Foxp3}}$ cells demonstrated lower ECAR and OCR than CAR-T$_{\text{Conv}}$ cells following GPC3 protein stimulation (Figures 1B and S1B). Using liquid chromatography-mass spectrometry (LC-MS), we assessed the metabolic flux of [U-C13]-glucose (Figures 1C, 1E, and S1C) and [U-C13]-glutamine (Figures 1D, 1F, and S1D) to examine metabolic behaviors of these CAR-T cells post GPC3 antigen stimulation. CAR-T$_{\text{Foxp3}}$ cells produced less (M + 3) lactate from [U-C13]-glucose, showing reductions in (M + 2) citrate and (M + 2) malate levels, than that in CAR-T$_{\text{Conv}}$ cells (Figure 1E). The [U-C13]-glutamine metabolic flux indicated reduced incorporation of glutamine into the tricarboxylic acid (TCA) cycle, as evidenced by lower levels of (M + 5) glutamate, (M + 4) malate, (M + 4) aspartate, and (M + 4) citrate in CAR-T$_{\text{Foxp3}}$ cells relative to those in CAR-T$_{\text{Conv}}$ cells (Figure 1F). Direct pyruvate addition did not restore the reduced ECAR and OCR levels in CAR-T$_{\text{Foxp3}}$ cells compared with those in CAR-T$_{\text{Conv}}$ cells (Figure S1E). Furthermore, we observed lower intracellular ATP levels and a higher NAD/NADH ratio in CAR-T$_{\text{Foxp3}}$ cells compared with those in CAR-T$_{\text{Conv}}$ cells (Figure 1G), indicating moderate downregulation of both glycolysis and OXPHOS in CAR-T$_{\text{Foxp3}}$ cells.

Next, we thoroughly investigated the metabolite composition using non-targeted LC-MS screening. We identified differentially expressed metabolites associated with lipid and amino acid metabolic pathways in the Kyoto Encyclopedia of Genes and Genomes (KEGG) database, highlighting pathways such as glycerophospholipid metabolism, sphingolipid metabolism, and glutathione metabolism, as well as aspartate and glutamate metabolism pathways (Figures S1F and S1G). Lipidomics further confirmed a significant increase in triglyceride levels in CAR-T$_{\text{Foxp3}}$ cells compared with those in CAR-T$_{\text{Conv}}$ cells (Figures 1H and S1H). BODIPY dye staining also indicated a substantial elevation in intracellular lipid droplet content in CAR-T$_{\text{Foxp3}}$ cells relative to that in CAR-T$_{\text{Conv}}$ cells (Figure 1I). Treatment with sodium dichloroacetate (DCA), known to enhance conversion of cytosolic pyruvate to mitochondrial acetyl-CoA and increase OXPHOS,[26,27] significantly reduced intracellular lipid droplet content in CAR-T$_{\text{Foxp3}}$ cells compared with that in untreated cells (Figure 1I), implying that Foxp3-mediated reduction in OXPHOS contributes to upregulation of lipid-related metabolism. Additionally, we noted an observable reduction in mitochondrial membrane potential (MMP) and mitochondrial mass in CAR-T$_{\text{Foxp3}}$ cells compared with those in CAR-T$_{\text{Conv}}$ cells (Figure 1J), indicating altered mitochondrial functions. Collectively, our data suggest that CAR-T$_{\text{Foxp3}}$ cells possess metabolic characteristics largely resembling those of Tregs[12–15] but distinct from those of CAR-T$_{\text{Conv}}$ cells.

Metabolic characteristics of CAR-T$_{\text{Foxp3}}$ cells are determined by Foxp3 binding to Drp1

Given alterations in MMP and mitochondrial mass, we investigated whether the metabolic pattern of CAR-T$_{\text{Foxp3}}$ cells resulted from the direct effect of Foxp3 on mitochondrial dynamics-related proteins, including optic atrophy 1 (Opa1), dynamin-related protein 1 (Drp1), mitofusin 1 (Mfn1), and mitofusin 2 (Mfn2).[28,29] Bimolecular fluorescence complementation (BiFC) experiments (Figure S2A) revealed interaction between Foxp3 and Drp1 but not with other mitochondrial dynamics-related proteins in HEK293T cells (Figures 2A and S2B). We further validated this interaction using a glutathione S-transferase (GST) pull-down assay in HEK293T cells (Figure 2B). Although Foxp3 is primarily recognized as a transcriptional regulator within the nucleus, further investigations have identified its presence in the cytoplasm.[30] Therefore, we generated Neongreen-Foxp3 and mCherry-Drp1 fusion proteins to explore their distribution in HEK293T cells (Figure S2C). Drp1 localized exclusively in the cytoplasm, whereas Foxp3 was present in both the cytoplasm and nucleus, corroborating its colocation with Drp1 in the cytoplasm (Figure 2C). Immunofluorescence of HEK293T cells helped confirm their colocalization in the cytoplasm (Figure 2D). We also validated this phenomenon in CAR-T cells, using purified circulating Tregs as a control. In CAR-T$_{\text{Foxp3}}$ cells,

downstream metabolites were produced by enzyme processes that rearranged carbon atoms. Figure 1C represented the specific labeled metabolites produced by [U-C13]-glucose through glycolysis and TCA cycle. Figure 1D depicted the specific labeled metabolites generated by [U-C13]-glutamine through TCA cycle.

(E) Analysis of [U-C13]-glucose derivatives, including (M + 6) fructose-1,6-bisphosphate (FBP), (M + 3) lactate, (M + 2) citrate, and (M + 2) malate in CAR-T$_{\text{Foxp3}}$ and CAR-T$_{\text{Conv}}$ cells ($n = 3$ biological replicates).

(F) Analysis of [U-C13]-glutamine derivatives, including (M + 5) glutamate, (M + 4) malate, (M + 4) aspartate, and (M + 4) citrate in CAR-T$_{\text{Foxp3}}$ and CAR-T$_{\text{Conv}}$ cells ($n = 3$ biological replicates).

(G) Quantification of intracellular ATP and NAD$^+$/NADH ratio in CAR-T$_{\text{Conv}}$ and CAR-T$_{\text{Foxp3}}$ cells ($n = 3$ independent volunteers).

(H) Triglyceride Z-score plot of CAR-T$_{\text{Foxp3}}$ cells vs. CAR-T$_{\text{Conv}}$ cells ($n = 5$ biological replicates).

(I) Quantification of intracellular lipid droplet gMFI in CAR-T$_{\text{Conv}}$ cells, CAR-T$_{\text{Foxp3}}$ cells, and CAR-T$_{\text{Foxp3}}$ cells treated with DCA ($n = 3$ independent volunteers).

(J) Representative flow plots and quantification of mitochondrial mass gMFI and MMP gMFI in CAR-T$_{\text{Conv}}$ and CAR-T$_{\text{Foxp3}}$ cells ($n = 3$ independent volunteers).

gMFI, geometric mean fluorescence intensity. MMP, mitochondrial membrane potential.

Data are presented as mean ± SD (B, E–G, I, and J). Statistical significance was calculated using unpaired Student's t tests (B, E–G, and J) and one-way ANOVA (I). NS, not significant, $^{*}p < 0.05$, $^{**}p < 0.01$, $^{***}p < 0.001$.

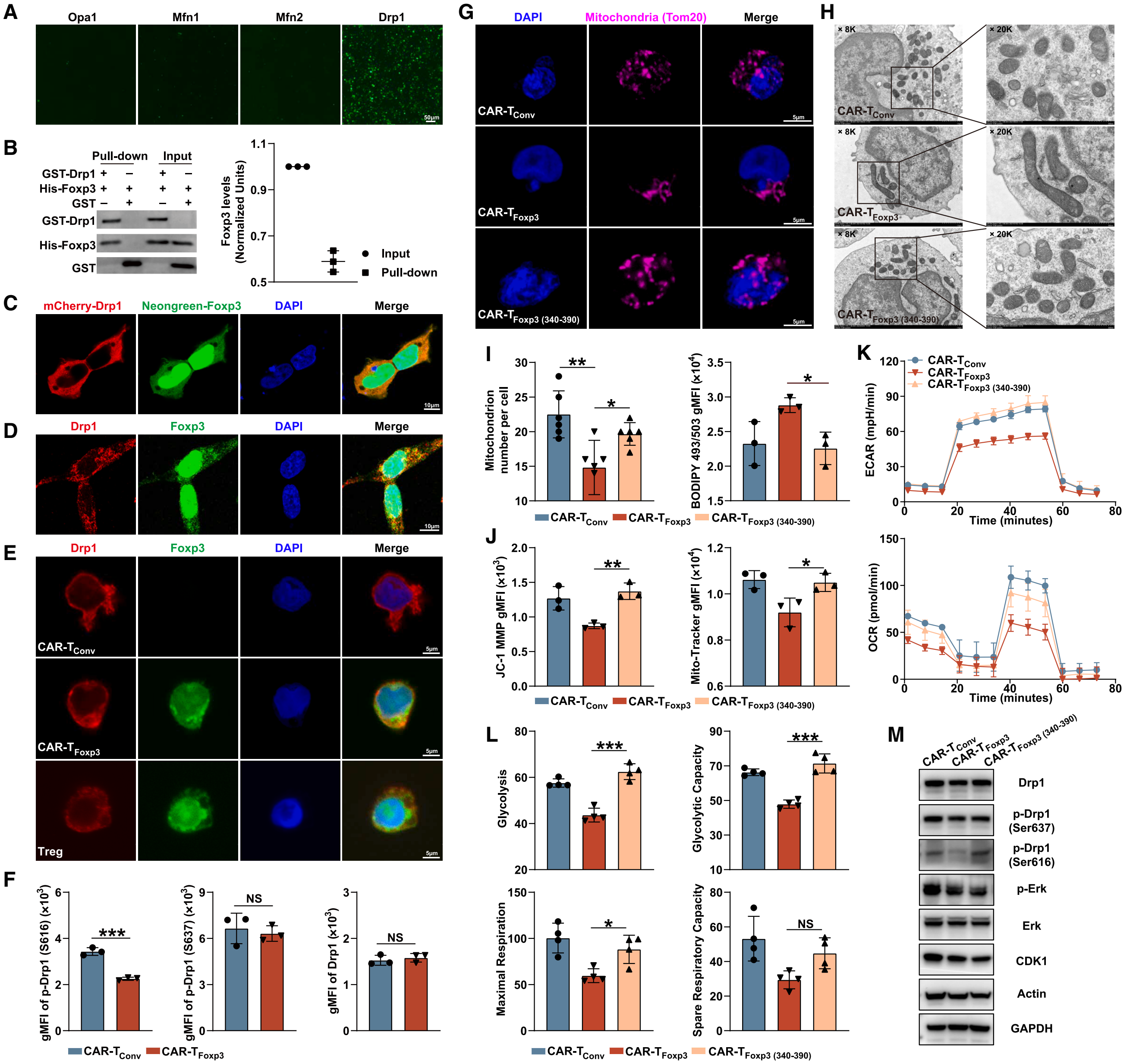

Figure 2. Metabolic characteristics of CAR-T$_{\text{Foxp3}}$ cells are determined by Foxp3 binding to Drp1

(A) Representative images of BiFC assay in HEK293T cells transfected with *Foxp3*-VC155 and one of the *Opa1*-VN173, *Mfn1*-VN173, *Mfn2*-VN173, and *Drp1*-VN173 plasmids; scale bar, 50 μm. Representative images from two independent experiments.

(B) Representative results and quantification of GST pull-down assay confirming the interactions between Drp1 and Foxp3 (*n* = 3 biological replicates). Representative images from three independent experiments.

(C) Representative confocal microscopy images of HEK293T cells transfected with Neongreen-*Foxp3* and mCherry-*Drp1* fusion plasmids; scale bar, 10 μm. Representative images from two independent experiments.

(D) Representative immunofluorescence images of HEK293T cells infected with GPC3-CAR-Foxp3 lentivirus; scale bar, 10 μm. Representative images from two independent experiments.

(E) Representative confocal microscopy images of Treg, CAR-T$_{\text{Foxp3}}$, and CAR-T$_{\text{Conv}}$ cells stained for DAPI, Drp1, and Foxp3; scale bar, 5 μm. Representative images from two independent experiments.

(F) Quantification of Drp1 expression and Drp1 phosphorylation at serine 616 and serine 637 in different CAR-T cells (*n* = 3 independent volunteers).

(G) Representative confocal microscopy images of CAR-T$_{\text{Conv}}$, CAR-T$_{\text{Foxp3}}$, and CAR-T$_{\text{Foxp3 (340–390)}}$ cells stained for DAPI and Tom20; scale bar, 5 μm. Representative images from two independent experiments.

(H) Representative electron microscope imaging of CAR-T$_{\text{Conv}}$, CAR-T$_{\text{Foxp3}}$, and CAR-T$_{\text{Foxp3 (340–390)}}$ cells. Representative results from two independent experiments.

(I) Quantification of mitochondrion number and intracellular lipid droplet gMFI in CAR-T$_{\text{Conv}}$, CAR-T$_{\text{Foxp3}}$, and CAR-T$_{\text{Foxp3 (340–390)}}$ cells (*n* = 3 independent volunteers).

(legend continued on next page)

Foxp3 exhibited cytoplasmic translocation and colocalization with Drp1, which also could be found in Tregs, whereas Foxp3 expression was undetectable in CAR-T_{Conv} cells (Figure 2E). Drp1-mediated mitochondrial fission is triggered by phosphorylation at serine 616, whereas fusion is facilitated by phosphorylation at serine 637.[31–33] Therefore, we analyzed Drp1 phosphorylation levels in CAR-T cells upon antigen stimulation using flow cytometry and western blotting. We observed that Foxp3 did not affect Drp1 expression or phosphorylation at serine 637 but significantly decreased phosphorylation at serine 616 (Figures 2F and 2M). AlphaFold software was used to predict the crystal structures of Foxp3 and Drp1 (Figure S2D). Foxp3-Drp1 docking results indicated that phosphorylation at serine 616 significantly increased the potential energy (from 16196.656 to 17679.332) and impacted the stability between Foxp3 and Drp1 (Figure S2E). Both confocal and electron microscopy indicated that, unlike the scattered mitochondria in CAR-T_{Conv} cells, those in CAR-T_{Foxp3} cells were clustered and elongated (Figures 2G and 2H). Moreover, the number of mitochondria in CAR-T_{Foxp3} cells was much fewer than that in CAR-T_{Conv} cells (Figure 2I). We also observed no obvious inhibitory effect of Foxp3 on the well-established upstream kinases (cyclin dependent kinase 1 [CDK1] and extracellular signal-regulated kinase 1/2 [ERK1/2]) of Drp1 (Figure 2M). These data indicate that the combination of Foxp3 and Drp1 might impair the Drp1 phosphorylation at serine 616 and mitochondrial fission to reprogram CAR-T cell metabolism.

Docking studies were performed using Schrödinger software to investigate the binding site between Foxp3 and Drp1. From 70,000 calculations, the top five poses (poses 11, 21, 18, 16, and 12) exhibiting the highest binding stability were selected (Figure S2F). Based on these predictions, we constructed various plasmids with partially deleted *Foxp3* sequences (Figure S2G). These plasmids were used at identical concentrations to ensure comparable expression levels in HEK293T cells (Figure S2H). The BiFC assay indicated disruption of the Foxp3-Drp1 interaction only when the fragment spanning amino acids 340–390 was deleted (Figure S2I). Subsequently, to investigate whether Foxp3 reprograms CAR-T_{Foxp3} cell metabolism via binding to Drp1, we established 340–390 fragment-deficient CAR-T_{Foxp3} cells (CAR-$T_{Foxp3\ (340–390)}$), which expressed similar levels of CAR and Foxp3 to CAR-T_{Foxp3} cells (Figure S2J). Following deletion of the 340–390 fragment, the fused mitochondria in CAR-T_{Foxp3} cells were eliminated (Figures 2G and 2H), and the reduced number of mitochondria was restored compared with CAR-T_{Conv} cells and CAR-T_{Foxp3} cells (Figure 2I). CAR-$T_{Foxp3\ (340–390)}$ cells also exhibited decreased lipid droplet content (Figure 2I), as well as increased mitochondrial mass, MMP, ECAR, and OCR, compared with that in CAR-T_{Foxp3} cells (Figures 2J–2L). Notably, deletion of the 340–390 fragment in Foxp3 did not alter expression levels of CDK1 or phospho-ERK1/2 but significantly enhanced Drp1 phosphorylation at serine 616 in CAR-$T_{Foxp3\ (340–390)}$ cells compared with that in CAR-T_{Foxp3} cells (Figure 2M). Based on the predicted protein-protein interaction site data, the 340–390 fragment of Foxp3 may bind to the 600–620 segment of Drp1 (Figure S2K). To validate this prediction, we constructed a Drp1 variant with the 600–620 fragment deleted. Compared with wild-type Drp1, this variant significantly reduced the mean fluorescence intensity of BiFC (Figure S2L), indicating the involvement of the 600–620 fragment of Drp1 in the interaction between Foxp3 and Drp1, which may also explain the downregulation of Drp1 phosphorylation at serine 616. Collectively, our findings suggest that the metabolic reprogramming of CAR-T_{Foxp3} cells is mediated by Foxp3 binding to Drp1.

CAR-T_{Foxp3} cells do not gain the chromatin accessibility and suppressive function of Tregs

Considering the critical role of Foxp3 in Treg development and differentiation, we determined whether CAR-T_{Foxp3} cells were converted to Tregs from the chromatin landscape. Therefore, we analyzed chromatin accessibility across the genome among Tregs, CAR-T_{Conv}, and CAR-T_{Foxp3} cells. We observed that assay for transposase-accessible chromatin with high-throughput sequencing (ATAC-seq) peaks were predominantly located in the promoter, intron, and distal intergenic regions (Figure S3A), and dimensionality reduction analysis effectively distinguished these cell types (Figure 3A). After aligning and removing duplicate and low-mapping-quality reads, we calculated the average ATAC-seq signals around transcription start sites (TSSs). These data indicated that Tregs exhibited lower read concentrations than those in the other two groups, whereas CAR-T_{Conv} and CAR-T_{Foxp3} cells exhibited similar ATAC-seq signals around TSSs (Figure 3B). Subsequent analysis using the R package DiffBind helped identify discriminating ATAC-seq peaks between Treg and CAR-T_{Conv} cells (Figure 3C). Peaks significantly elevated in Tregs were highly enriched in motifs recognized by transcriptional repressor GATA binding 1 (TRPS1), RUNX family transcription factor 2 (RUNX2), basic leucine zipper ATF-like transcription factor (BATF), ETS-related gene (ERG), and MYB proto-oncogene like 2 (BMYB) transcription factors (Figure 3D), some of which have been reported to engage in the inhibitory function of Tregs.[34–36] However, these peaks were not enriched in CAR-T_{Foxp3} cells, highlighting a fundamental difference in chromatin landscape between CAR-T_{Foxp3} and Treg cells (Figure 3E). We then analyzed Treg cell-related markers and cytokines in CAR-T_{Conv}, CAR-T_{Foxp3}, Treg, and conventional T (T_{Conv}) cells. Compared with Tregs, CAR-T_{Foxp3} cells secreted lower levels of interleukin-10 (IL-10) and transforming growth factor β (TGF-β) and expressed

---

(J) Quantification of mitochondrial mass gMFI and MMP gMFI in CAR-T_{Conv}, CAR-T_{Foxp3}, and CAR-$T_{Foxp3\ (340–390)}$ cells ($n = 3$ independent volunteers).

(K) ECAR and OCR of CAR-T_{Conv}, CAR-T_{Foxp3}, and CAR-$T_{Foxp3\ (340–390)}$ cells ($n = 4$ biological replicates). Representative results from two independent experiments.

(L) Quantification of (K).

(M) Western blot analysis of Drp1, p-Drp1(S616), p-Drp1(S637), Erk, p-Erk, and CDK1 in different CAR-T cells.

gMFI, geometric mean fluorescence intensity. MMP, mitochondrial membrane potential.

Data are presented as mean ± SD (F and I–L). Statistical significance was calculated using unpaired Student's t tests (F) and one-way ANOVA (I, J, and L). NS, not significant, $^*p < 0.05$, $^{**}p < 0.01$, $^{***}p < 0.001$.

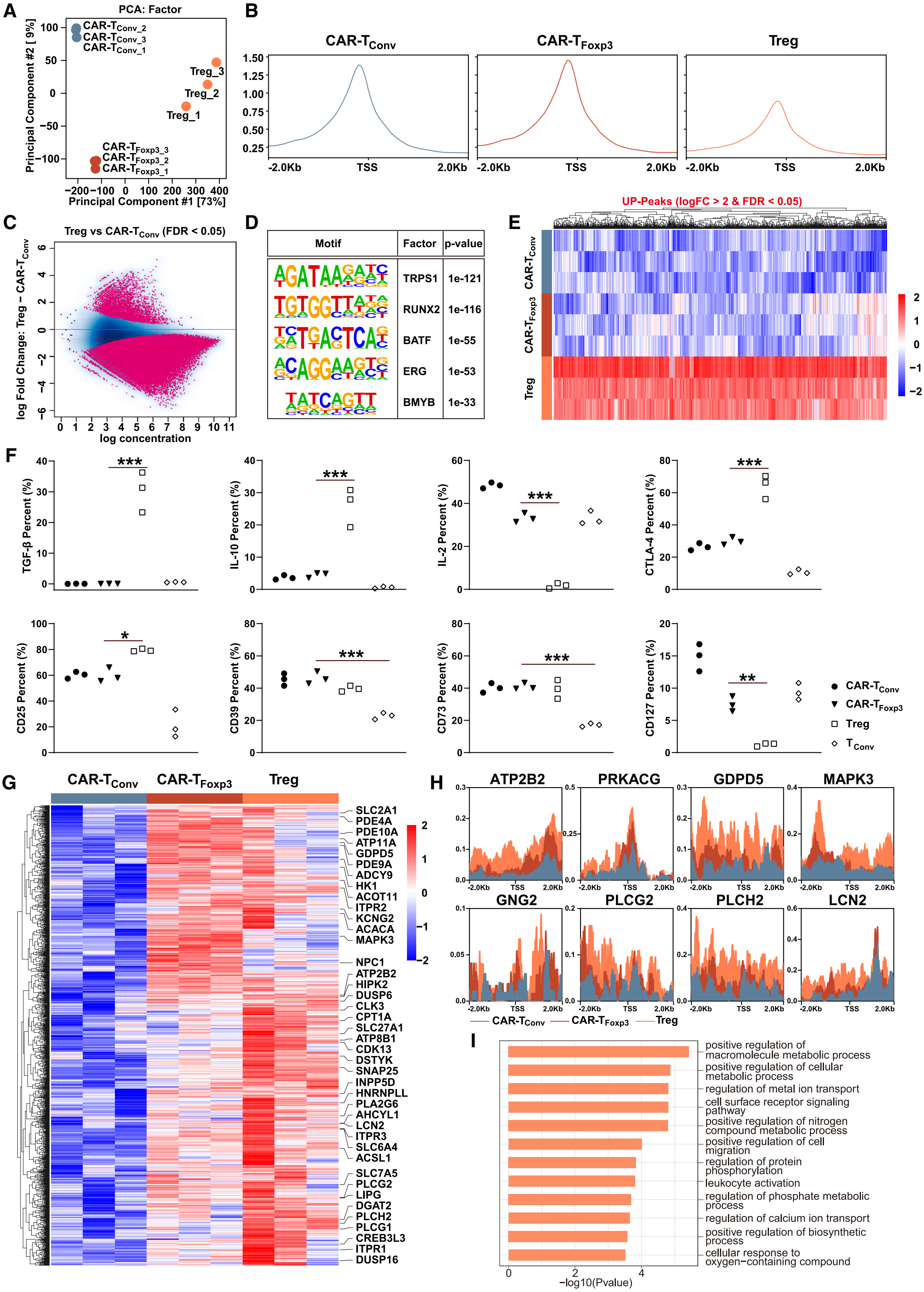

Figure 3. CAR-T$_{\text{Foxp3}}$ cells do not gain the chromatin accessibility and suppressive function of Tregs

(A) Principal-component analysis (PCA) analysis of ATAC-seq data for CAR-T$_{\text{Foxp3}}$, CAR-T$_{\text{Conv}}$, and Treg cells from the same donor (*n* = 3 biological replicates).

(B) Representative enrichment scores of ATAC-seq data across TSSs +/− 2 kb.

(legend continued on next page)

reduced levels of the cytotoxic T-lymphocyte associated protein 4 (CTLA-4) inhibitory receptor, which aligned closely with CAR-T$_{\text{Conv}}$ cells (Figure 3F). Expressions of CD39 and CD73 among CAR-T$_{\text{Foxp3}}$, CAR-T$_{\text{Conv}}$, and Treg cells did not significantly differ following GPC3 antigen stimulation (Figure 3F). We further investigated the suppressive effect of CAR-T$_{\text{Foxp3}}$ cells on T$_{\text{Conv}}$ cell proliferation by co-culturing CAR-T$_{\text{Conv}}$, CAR-T$_{\text{Foxp3}}$, or Treg cells with carboxyfluorescein diacetate succinimidyl ester (CFSE)-labeled naive T$_{\text{Conv}}$ cells under Dynabeads stimulation. T$_{\text{Conv}}$ cell proliferation in the CAR-T$_{\text{Foxp3}}$ group was significantly stronger than that in the Treg group but almost identical to that in the CAR-T$_{\text{Conv}}$ group (Figure S3B), suggesting an absence of inhibitory effect in CAR-T$_{\text{Foxp3}}$ cells. Only a few peaks upregulated in CAR-T$_{\text{Foxp3}}$ but downregulated in CAR-T$_{\text{Conv}}$ cells were co-enriched in Tregs (Figures 3G and 3H). Pathway enrichment analysis revealed that these peaks concentrated in cellular metabolic processes, such as the positive regulation of biosynthetic processes, macromolecular metabolic processes, and nitrogen compound metabolic processes (Figure 3I). Given the reported epigenetic regulatory functions of cellular metabolites,[37–39] we used mass spectrometry to detect metabolites in CAR-T$_{\text{Conv}}$ and CAR-T$_{\text{Foxp3}}$ cells. The results indicated significantly lower levels of lactate, fumarate, and NADH in CAR-T$_{\text{Foxp3}}$ cells than those in CAR-T$_{\text{Conv}}$ cells (Figure S3C), potentially explaining the changes in chromatin accessibility associated with cellular metabolism in CAR-T$_{\text{Foxp3}}$ cells. These findings underscore a fundamental difference in the chromatin landscape and inhibitory effects of CAR-T$_{\text{Foxp3}}$ cells compared with those of Tregs.

Foxp3-mediated metabolism downregulates the expression of exhaustion-associated inhibitory molecules in CAR-T$_{\text{Foxp3}}$ cells

We next explored whether Foxp3-mediated metabolism contributes to CAR-T$_{\text{Foxp3}}$ cell activation and function. We incubated CAR-T$_{\text{Foxp3}}$ and CAR-T$_{\text{Conv}}$ cells with GPC3$^+$ Huh7 tumor cells for 72 h. We assessed activation markers (CD27, CD28, and CD69), phenotypic markers (CD45RA, CD62L, and CD95), and key transcription factors (B cell lymphoma 6 [BCL-6], eomesodermin [EOMES], and T cell factor 1 [TCF-1]) using spectral flow cytometry. High-dimensional, multicolor spectral flow data were visualized using T-distributed stochastic neighbor embedding (tSNE) methodology (Figure 4A). CAR-T$_{\text{Foxp3}}$ cells exhibited higher levels of CD27, CD28, CD62L, and BCL-6 and lower levels of CD95 and EOMES, as well as slightly lower TCF-1 compared with those in CAR-T$_{\text{Conv}}$ cells (Figure 4B). Cytotoxicity evaluations, including a CCK8-based assay (Figure S4A), videos (Video S1 and Video S2), and the fluorescence intensity change curve (Figure 4C) of live cell imaging, demonstrated that CAR-T$_{\text{Foxp3}}$ cells exhibited a consistent killing ability similar to that of CAR-T$_{\text{Conv}}$ cells. Moreover, after GPC3 antigen stimulation, CAR-T$_{\text{Foxp3}}$ cells released fewer cytokines (granzyme B, interferon [IFN]-γ, and tumor necrosis factor [TNF]-α) than those released by CAR-T$_{\text{Conv}}$ cells (Figure 4D). Following 72 h of GPC3 tumor antigen stimulation, CAR-T$_{\text{Foxp3}}$ cells expressed lower percentages of programmed cell death-1 (PD-1), lymphocyte activation gene-3 (LAG-3), and T cell immunoglobulin domain and mucin domain-3 (TIM-3) and displayed less triple or double positivity for these exhaustion markers compared with those of CAR-T$_{\text{Conv}}$ cells (Figures 4E and 4F). Nonetheless, exhaustion marker levels in CAR-T$_{\text{Foxp3 (340–390)}}$ cells were higher than those in CAR-T$_{\text{Foxp3}}$ cells but similar to or slightly lower than those in CAR-T$_{\text{Conv}}$ cells (Figure 4F). We subjected CAR-T cells to GPC3 antigen stimulation every 4 days across three rounds to evaluate the persistence and exhaustion of CAR-T cells (Figure S4B). CAR-T$_{\text{Foxp3}}$ cells outnumbered CAR-T$_{\text{Conv}}$ cells on days 4 and 8 (Figure S4C). By day 12, a significant decrease in exhaustion molecules (PD-1 and TIM-3) and an increase in the stem cell marker (CD62L) were observed in CAR-T$_{\text{Foxp3}}$ cells compared with those in CAR-T$_{\text{Conv}}$ cells (Figures 4G and S4D). However, this decrease in exhaustion markers and increase in cell number in CAR-T$_{\text{Foxp3}}$ cells were not maintained in CAR-T$_{\text{Foxp3 (340–390)}}$ cells after 12 days of antigen stimulation (Figures 4G and S4C). We then pre-treated CAR-T$_{\text{Conv}}$ and CAR-T$_{\text{Foxp3}}$ cells with P110, which bound directly to Drp1 and significantly increased the phosphorylation of Drp1 at serine 616 (Figure S4E). The percentages of PD-1, LAG-3, and TIM-3 increased significantly in P110-pre-treated CAR-T$_{\text{Foxp3}}$ cells compared with those without P110 treatment (Figure 4H), whereas no differences were observed between CAR-T$_{\text{Conv}}$ cells with and without P110 (Figure 4H). These data suggest that both Foxp3-mediated interactions with Drp1 and p-Drp1 impairment contribute to the downregulation of exhaustion markers in CAR-T$_{\text{Foxp3}}$ cells. Additionally, we examined whether the reduced exhaustion markers in CAR-T$_{\text{Foxp3}}$ cells were associated with Foxp3-mediated metabolic patterns. We treated CAR-T$_{\text{Conv}}$ and CAR-T$_{\text{Foxp3}}$ cells with DCA upon GPC3 stimulation. Flow cytometry results indicated that exhaustion marker percentages significantly increased after adding DCA in CAR-T$_{\text{Foxp3}}$ cells but not in CAR-T$_{\text{Conv}}$ cells (Figure 4I). Furthermore, trimetazidine-induced inhibition of long-chain 3-ketoyl coenzyme A thiolase, which is involved in fatty acid β-oxidation, significantly increased the expression of exhaustion markers (TIM-3 and LAG-3) in CAR-T$_{\text{Foxp3}}$ cells but not in CAR-T$_{\text{Conv}}$ cells (Figure S4F). Collectively, these results suggest that Foxp3-mediated metabolism does not affect cytotoxicity but downregulates the expression of inhibitory molecules linked to exhaustion in CAR-T$_{\text{Foxp3}}$ cells.

(C) Differential peaks plot between CAR-T$_{\text{Conv}}$ cells and Tregs identified by the DiffBind package ($n = 3$ biological replicates).
(D) Top five motifs and factors enriched in Treg cell highly elevated peaks using Homer software ($\text{LogFC} > 2$ and $\text{FDR} < 0.05$).
(E) Heatmap of Treg cell highly elevated peaks ($\text{LogFC} > 2$ and $\text{FDR} < 0.05$) in CAR-T$_{\text{Conv}}$ and CAR-T$_{\text{Foxp3}}$ cells.
(F) Quantification of Treg-related cytokines and markers in CAR-T$_{\text{Conv}}$, CAR-T$_{\text{Foxp3}}$, Treg, and T$_{\text{Conv}}$ cells ($n = 3$ independent volunteers).
(G) Heatmap of peaks were co-enriched in Treg and CAR-T$_{\text{Foxp3}}$ cells.
(H) Enrichment score profile of representative genes, which are derived from (G).
(I) Enriched Gene Ontology (GO) terms for peaks co-enriched in Treg and CAR-T$_{\text{Foxp3}}$ cells.
PCA, principal-component analysis; FDR, false discovery rate.
Data are presented showing all individual data points (F). Statistical significance was calculated using one-way ANOVA (F). *$p < 0.05$, **$p < 0.01$, ***$p < 0.001$.

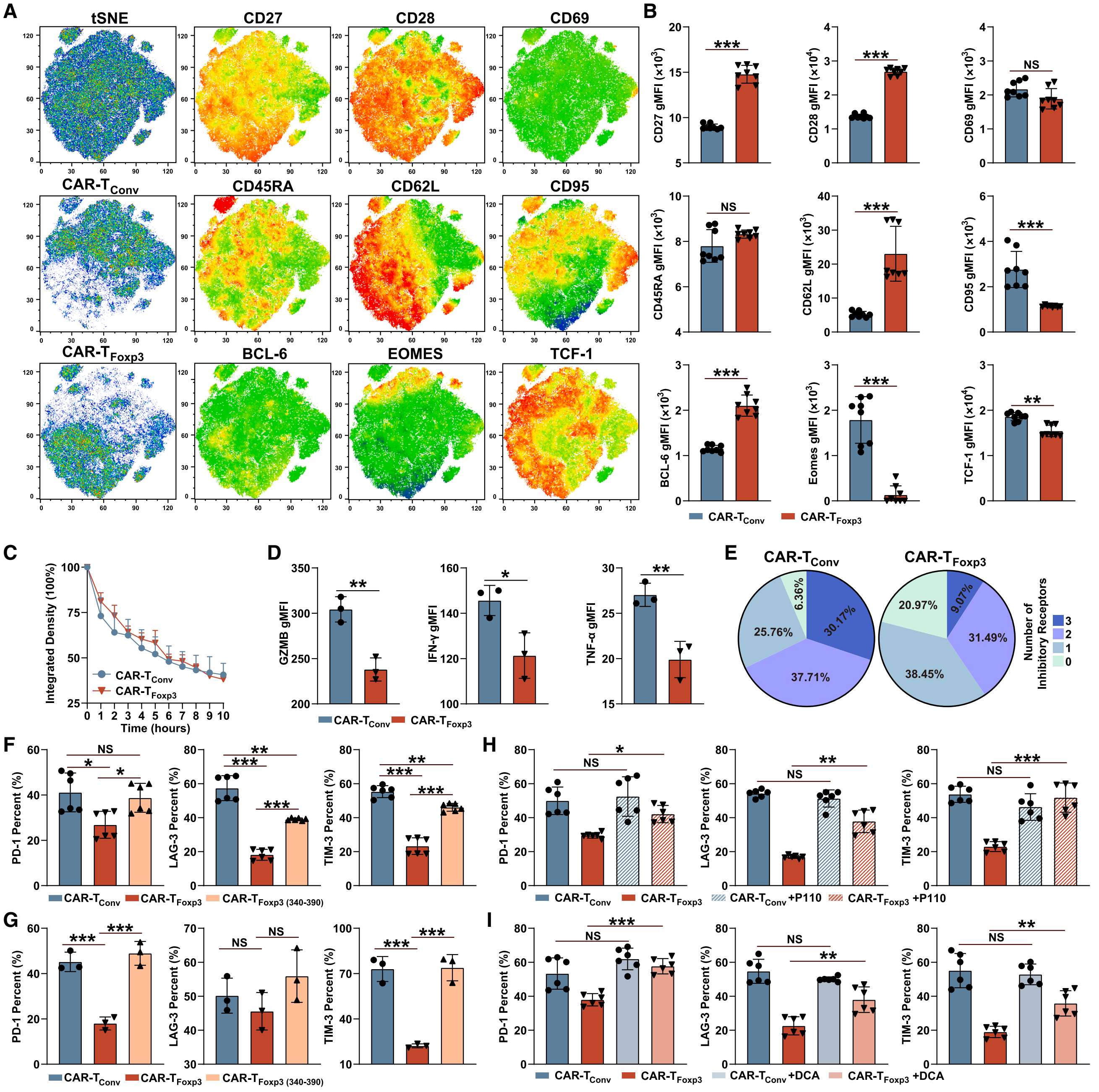

Figure 4. Foxp3-mediated metabolism downregulates the expression of exhaustion-associated inhibitory molecules in CAR-T$_{Foxp3}$ cells

(A) Activation markers (CD27, CD28, CD69), phenotype markers (CD45RA, CD62L, CD95), and transcription factors (BCL-6, TCF-1, EOMES) of CAR-T$_{Foxp3}$ and CAR-T$_{Conv}$ cells were analyzed via spectral flow cytometry 3 days after antigen-specific stimulation and depicted as tSNE plots (*n* = 2 donors in quadruplicate).

(B) Quantification of (A).

(C) The fluorescence intensity change curve of live cell imaging for evaluating cytotoxic activity of different CAR-T cells against hepatocellular carcinoma cell line Huh7 at an E/T ratio of 4:1 (*n* = 3 biological replicates).

(D) Quantification of granzyme B (GZMB) gMFI, IFN-γ gMFI, and TNF-α gMFI in CAR-T$_{Foxp3}$ and CAR-T$_{Conv}$ cells after co-culture with Huh7 cells for 6 h (*n* = 3 independent volunteers).

(E) Quantification of triple or double positivity for PD-1, TIM-3, and LAG-3 receptors on different CAR-T cells after antigen-specific stimulation (*n* = 2 donors in triplicate). To plot the pie chart, CAR-T cells were specifically stimulated for 3 days, and the expression of inhibitory receptors was analyzed and counted, where PD-1$^+$TIM-3$^+$LAG-3$^+$ indicated 3-positive and PD-1$^-$TIM-3$^-$LAG-3$^-$ indicated 3-negative.

(F) Quantification of exhaustion markers on CAR-T$_{Conv}$, CAR-T$_{Foxp3}$, and CAR-T$_{Foxp3\ (340–390)}$ cells after antigen-specific stimulation for 3 days (*n* = 2 donors in triplicate).

(G) Quantification of exhaustion markers on CAR-T$_{Conv}$, CAR-T$_{Foxp3}$, and CAR-T$_{Foxp3\ (340–390)}$ cells in the end of three rounds of GPC3 antigen stimulation *in vitro* (*n* = 3 independent volunteers).

(legend continued on next page)

CAR-T_{Foxp3} cells exhibit potent antitumor activity with reduced exhaustion markers *in vivo*

To determine whether CAR-T_{Foxp3} cells could display enhanced antitumor ability *in vivo*, we established a subcutaneous xenograft tumor model in mice. Untransduced T cells or various CAR-T cells were injected on day 8, when tumors reached approximately 100 mm^3 (Figure 5A). Tumor growth curves (Figures 5B and 5C) indicated that mice treated with CAR-T_{Foxp3} cells exhibited the slowest tumor growth, confirmed by tumor weight (Figure 5D). We harvested tumors from each group for flow cytometry analysis on day 20 and observed that CD28 expression was markedly increased, and exhaustion markers (PD-1, LAG-3, and TIM-3) were markedly decreased in CAR-T_{Foxp3} cells compared with those in CAR-T_{Conv} cells (Figures 5E, 5G, and S5A). Moreover, the triple or double positivity for PD-1, TIM-3, and LAG-3 receptors was substantially less in CAR-T_{Foxp3} cells (Figure 5F). Confocal immunofluorescence analyses showed that the ratio of PD-1 integrated density (IntDen) to CD3 IntDen was markedly reduced in tumor-infiltrating CAR-T_{Foxp3} cells compared with that in CAR-T_{Conv} cells (Figures 5H and 5I).

For further analysis, we conducted RNA sequencing (RNA-seq) on tumor-infiltrating CAR-T_{Foxp3} or CAR-T_{Conv} cells post-fluorescence-activated cell sorting. Principal-component analysis distinguished CAR-T_{Foxp3} from CAR-T_{Conv} cells significantly (Figure S5B). Foxp3 expression was persistently elevated, whereas the expression of TIM-3, LAG-3, EOMES, and CXCL13 was significantly downregulated in CAR-T_{Foxp3} cells compared with those in CAR-T_{Conv} cells (Figures 5J and S5C). Gene set enrichment analysis (GSEA) showed that CAR-T_{Foxp3} cells were in a lower exhaustion state than that of CAR-T_{Conv} cells (Figure 5K). Tregs and CD4$^+$ T_{Conv} cells were included in the analysis, and the upregulated genes of Tregs were identified (Figure S5D). The expression of these genes in Tregs was significantly different from those in CAR-T_{Foxp3} and CAR-T_{Conv} cells (Figure S5E), indicating the fact that tumor-infiltrating CAR-T_{Foxp3} cells and Tregs were fundamentally different at the transcriptome level. Moreover, some upregulated genes in CAR-T_{Foxp3} cells overlapped with Tregs and were enriched for cellular metabolic pathways (Figure 5L), supporting similar metabolic characteristics of tumor-infiltrating CAR-T_{Foxp3} cells to Tregs. Pathways related to mitochondria were also significantly enriched in CAR-T_{Foxp3} cells compared with that in CAR-T_{Conv} cells (Figure S5F). Among the well-defined target genes of Foxp3,[40] only *IFNG* was downregulated, whereas *KLF2*, *TRIB2*, *S1PR1*, *SELL*, and *ZC3H12D* were upregulated in CAR-T_{Foxp3} cells (Figure S5G), highlighting the partially distinct roles of Foxp3 in CAR-T_{Foxp3} cells and Tregs. These results suggest that CAR-T_{Foxp3} cells exhibit a more potent antitumor ability and lower exhaustion-associated inhibitory molecules than those of CAR-T_{Conv} cells.

Foxp3 sustains long-lasting antitumor effects and low levels of exhaustion markers in CAR-T_{Foxp3} cells *in vivo*

To investigate whether Foxp3-mediated metabolism contributes to the antitumor effects of CAR-T cells, we established a tumor rechallenge model. CAR-T cells were administered preemptively when tumors measured 50 mm^3 on day 4 (Figure 6A). All tumors were eliminated, with the CAR-T_{Foxp3} group showing slightly faster tumor clearance than that of the CAR-T_{Conv} group (Figure 6B). After the initial tumor clearance on day 25, no differences in peripheral blood CAR-T cell counts were observed between CAR-T_{Conv} and CAR-T_{Foxp3} cells (Figure 6C). Notably, compared with CAR-T_{Conv} cells, CAR-T_{Foxp3} cells exhibited a higher percentage of naive/stem cell memory T (TN/TSCM) cells and a lower percentage of terminal effector memory T (TEMRA) cells (Figures 6D and 6E). Additionally, CAR-T_{Foxp3} cells showed a slightly higher central memory (TCM) or lower effector memory (TEM) and TEMRA than that of CAR-T_{Conv} cells before tumor challenge (Figures S6A and S6B). On day 29, cured mice from various CAR-T cell groups were rechallenged with 8 × 10^6 Huh7 tumor cells (Figure 6A), with tumor growth being the slowest in the CAR-T_{Foxp3} group (Figure 6F).

Further, to validate the role of Foxp3 in antitumor activity *in vivo*, we injected CAR-$T_{Foxp3\ (340–390)}$, CAR-T_{Foxp3}, and CAR-T_{Conv} cells into Huh7-bearing mice (Figure 6G). Tumor elimination was swift in all groups (Figure 6H). On day 29, cured mice from all groups were rechallenged with 8 × 10^6 Huh7 tumor cells, and the tumor volume was monitored throughout the experiment (Figure 6G). Tumor growth curves (Figure 6I) showed that the growth rates in mice treated with CAR-$T_{Foxp3\ (340–390)}$ cells were similar to those in the CAR-T_{Conv} group but faster than those in the CAR-T_{Foxp3} group, as confirmed by tumor volume and weight (Figure S6C). The percentages of TIM-3 and LAG-3 in the CAR-$T_{Foxp3\ (340–390)}$ group matched those in the CAR-T_{Conv} group but were much higher than those in the CAR-T_{Foxp3} group (Figure S6D). These findings confirm that the enhanced antitumor effect and reduced exhaustion-associated inhibitory molecules of CAR-T_{Foxp3} cells depend on Foxp3 residues 340–390.

CAR-T_{Foxp3} cells acquire potent antitumor activity but not immune suppression in humanized NSG models

To evaluate the antitumor effect of CAR-T_{Foxp3} cells in an immunocompetent model and their impact on other immune cells, we constructed human immune system reconstituted (humanized) NOD.Cg-Prkdc^{scid}Il2rg^{em1Smoc} (NSG) mice using CD34$^+$ hematopoietic stem cells. We detected various human immune cells, including T cells, B cells, natural killer (NK) cells, dendritic cells (DCs), and monocytes, in the peripheral blood and spleens of these mice (Figures S7A and S7B). In the peripheral blood, the average ratio of human immune cells (hCD45$^+$) to total immune cells (hCD45$^+$ or mCD45$^+$) exceeded 60%, and the ratio of human immune cells to living cells could even reach 80% in spleens

---

(H) Quantification of exhaustion markers on CAR-T_{Conv} and CAR-T_{Foxp3} cells after antigen-specific stimulation for 3 days in the presence or absence of P110 (n = 2 donors in triplicate).

(I) Quantification of exhaustion markers on CAR-T_{Conv} and CAR-T_{Foxp3} cells after antigen-specific stimulation for 3 days in the presence or absence of DCA (n = 2 donors in triplicate).

tSNE, t-distributed stochastic neighbor embedding; GZMB, granzyme B; IFN, interferon; TNF, tumor necrosis factor.

Data are presented as mean ± SEM (C) or SD (B, D, and F–I). Statistical significance was calculated using unpaired Student's t tests (B and D), one-way ANOVA (F–I), and two-way ANOVA (C). NS, not significant, $^*p < 0.05$, $^{**}p < 0.01$, $^{***}p < 0.001$.

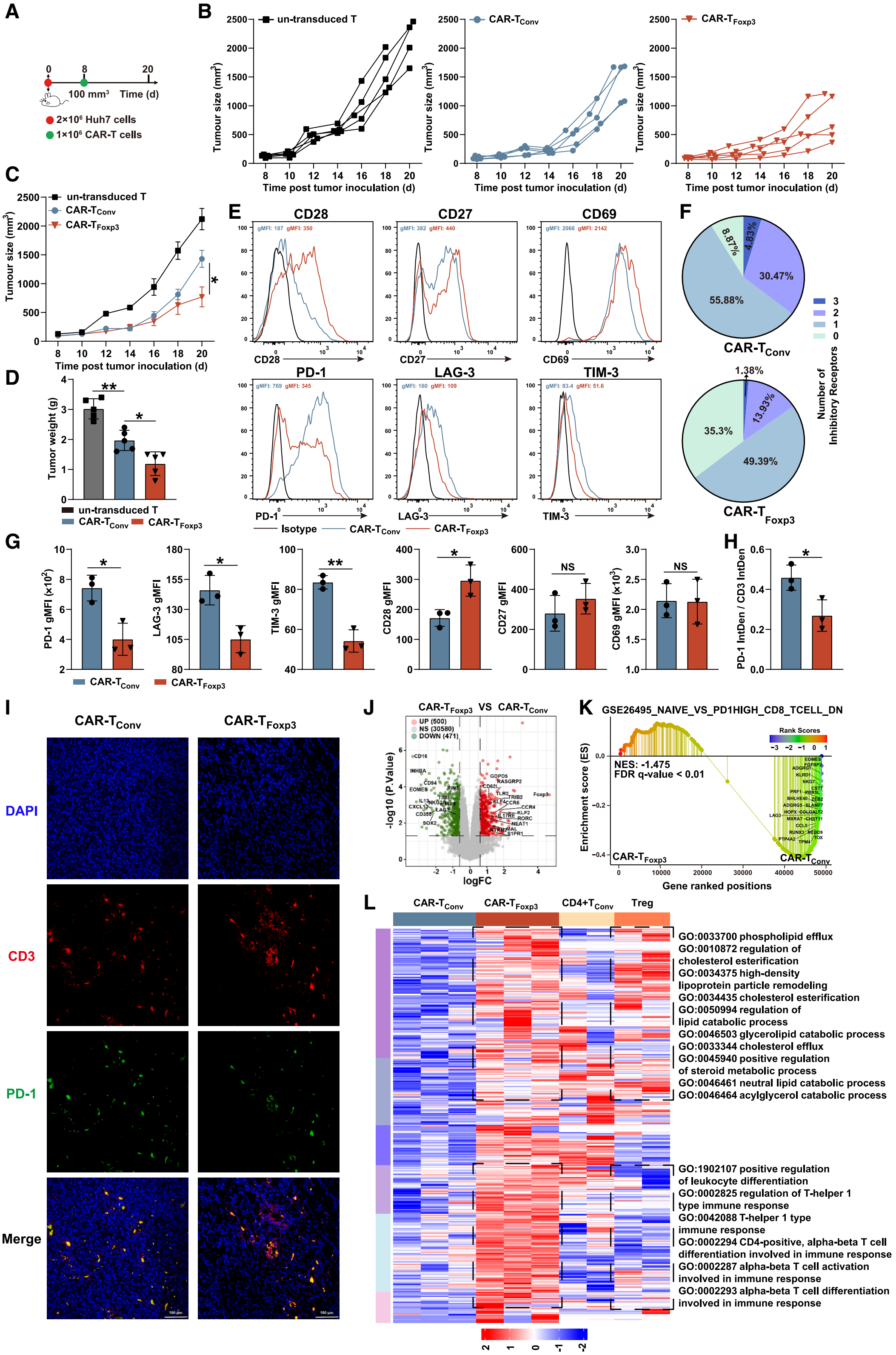

Figure 5. CAR-T$_{Foxp3}$ cells exhibit potent antitumor activity with reduced exhaustion markers *in vivo*

(A) Experimental timeline of the cell line-derived xenograft (CDX) tumor model.

(B and C) Time-dependent changes in tumor volume after tail vein injection of different CAR-T cells (*n* = 5 mice per group).

(legend continued on next page)

(Figures S7A and S7B). We established a subcutaneous xenograft tumor model and administered various CAR-T cells for treatment (Figure 7A). Tumor growth curves demonstrated that CAR-T_{Foxp3} cells effectively inhibited tumor growth, achieving complete remission in two out of five mice and significantly reducing tumor sizes in the remaining three mice compared with the untransduced T cell and CAR-T_{Conv} groups (Figures 7B and 7C). On day 25, we harvested and analyzed tumor-infiltrating CAR-T cells and other immune cells via flow cytometry. Compared with CAR-T_{Conv} group, CAR-T_{Foxp3} cells exhibited lower levels of exhaustion-associated inhibitory molecules (PD-1 and LAG-3) and higher tumor infiltration of $CD4^+$ T cells (Figures 7D and 7F). The compositions of tumor-infiltrating human immune cells ($CD8^+$ T cells, B cells, NK cells, cDC cells, and monocytes) in the CAR-T_{Foxp3} group were like those in the CAR-T_{Conv} group (Figure 7F). Furthermore, we noted no significant differences in spleen weight and vital organs of mice between the two groups (Figures 7E and S7C). Multiplex cytokine detection in peripheral blood indicated that TNF-α and IL-10 secretions were much lower in the CAR-T_{Foxp3} group than in the CAR-T_{Conv} group (Figure 7G). Unlike the varying cytokine levels within the CAR-T_{Conv} group, cytokine levels in the CAR-T_{Foxp3} group remained stable. Although not statistically significant, mean levels of IL-1β, IL-4, IL-6, IL-12p70, and IFN-γ in CAR-T_{Conv} group were notably higher than those in the CAR-T_{Foxp3} group (Figure 7G), suggesting a reduced cytokine storm following Foxp3 modification in CAR-T cells. Moreover, the concentration of IL-2, a crucial cytokine for the activation and proliferation of CAR-T cells, did not differ significantly between the groups (Figure 7G). These findings indicate that CAR-T_{Foxp3} cells not only demonstrate enhanced antitumor activity but also maintain safety without inducing immune suppression in humanized NSG models.

DISCUSSION

CAR-T cells are susceptible to exhaustion in the TME, which is considered a major obstacle in CAR-T cell therapy. Considering that immunosuppressive Tregs can thrive inside solid tumors and promote tumor progression,[41,42] we aimed to mimic Treg metabolism in CAR-T cells to overcome TME and prevent CAR-T cell exhaustion. Here, we demonstrated that overexpressing Foxp3 in CAR-T cells is an extremely efficient metabolic intervention that depends on the interaction of Foxp3 with Drp1. Furthermore, modification of the CAR-T cell metabolic pattern directly avoids tumor-infiltrating CAR-T cell exhaustion, boosts their cytotoxic capabilities, and improves their long-term immunosurveillance functions.

Tregs can survive, expand, and function in most solid tumors owing to their metabolic advantages; however, the metabolic pathways of Tregs remain controversial. Some studies have reported that Tregs exhibit lower OXPHOS and glycolysis levels, and increasing OXPHOS impairs Treg differentiation.[12–15] Whereas other studies have suggested that TGF-β-induced Tregs exhibit a high level of OXPHOS, enabling them to possess metabolic advantages in low-glucose, lactate-rich environments.[23,24,43] It has been reported that the costimulatory domains of CARs are involved in CAR-T cell metabolism, with the CD28 domain favoring glycolysis via mTOR signaling and the 4-1BB domain enhancing OXPHOS through AMPK activation.[44–46] The metabolic profiles of third-generation CAR-T cells co-expressing CD28 and 4-1BB domains remain unclear, potentially distinct from second-generation CAR-T cells given their demonstrated superior efficacy.[25] In this study, we found Foxp3 could interact with Drp1 and affect mitochondrial function and morphology. Mitochondria undergo fission and expansion after CAR-T cells are activated, and mitochondrial fission requires the participation of Drp1. Foxp3 may limit mitochondrial fission, reducing mitochondrial number, mitochondrial mass, and MMP, which may be the reason for decreased OXPHOS in CAR-T_{Foxp3} cells. Besides, Tregs have also been shown to exhibit increased lipid uptake and upregulate lactic acid metabolic pathways to maintain their suppressive capabilities.[21,22,47] Despite the controversial metabolic patterns, Tregs have a metabolic advantage within solid tumors. Foxp3 is constitutively expressed in Tregs and contributes to both metabolic regulation and Treg commitment. In the absence of Foxp3, Tregs lose their suppressor function.[48] In addition, Foxp3 strengthens the stability and molecular characteristics of the Treg lineage, including anergy and the inability to produce cytokine IL-2.[40] Clinically, *Foxp3* mutation causes immune dysregulation, polyendocrinopathy, enteropathy, and X-linked syndrome, which is caused by a lack of suppressive functional Tregs.[49] According to our RNA-seq and ATAC-seq results, overexpressing Foxp3 in CAR-T cells only changed the metabolic pathway—not the expression and chromatin accessibility of Treg inhibitory function-related genes.

(D) Huh7 tumor weight on day 20 (n = 5 mice per group).

(E) Representative flow plots of activation and exhaustion markers on tumor-infiltrating CAR-T cells isolated from the Huh7 tumor on day 20 (n = 3 biological replicates).

(F) Quantification of triple or double positivity for PD-1, TIM-3, and LAG-3 receptors on tumor-infiltrating CAR-T cells on day 20. To plot the pie chart, we set up three independent mice to calculate the mean values and plotted pie charts.

(G) Quantification of (E).

(H) Quantification of PD-1 IntDen/CD3 IntDen ratio (n = 3 biological replicates).

(I) Representative confocal immunofluorescence microscopy images of Huh7 tumor stained for DAPI, CD3, and PD-1; scale bar, 100 μm (n = 3 biological replicates).

(J) Differentially expressed gene volcano plot between tumor-infiltrating CAR-T_{Foxp3} cells and CAR-T_{Conv} cells identified by the limma package (n = 3 biological replicates).

(K) GSEA plot showing enrichment of PD-1^{high} $CD8^+$ T cell signature genes in CAR-T_{Conv} cells compared with CAR-T_{Foxp3} cells.

(L) Heatmap and enriched Gene Ontology (GO) terms for CAR-T_{Foxp3} cell highly elevated genes across several groups (CAR-T_{Conv} cells, n = 3 biological replicates; CAR-T_{Foxp3} cells, n = 3 biological replicates; $CD4^+$ T_{Conv} cells, n = 2 biological replicates; Tregs, n = 2 biological replicates).

Data are presented as mean ± SEM (C) or SD (D, G, and H). Statistical significance was calculated using unpaired Student's t tests (G and H), one-way ANOVA (D), and two-way ANOVA (C). NS, not significant, $^*p < 0.05$, $^{**}p < 0.01$.

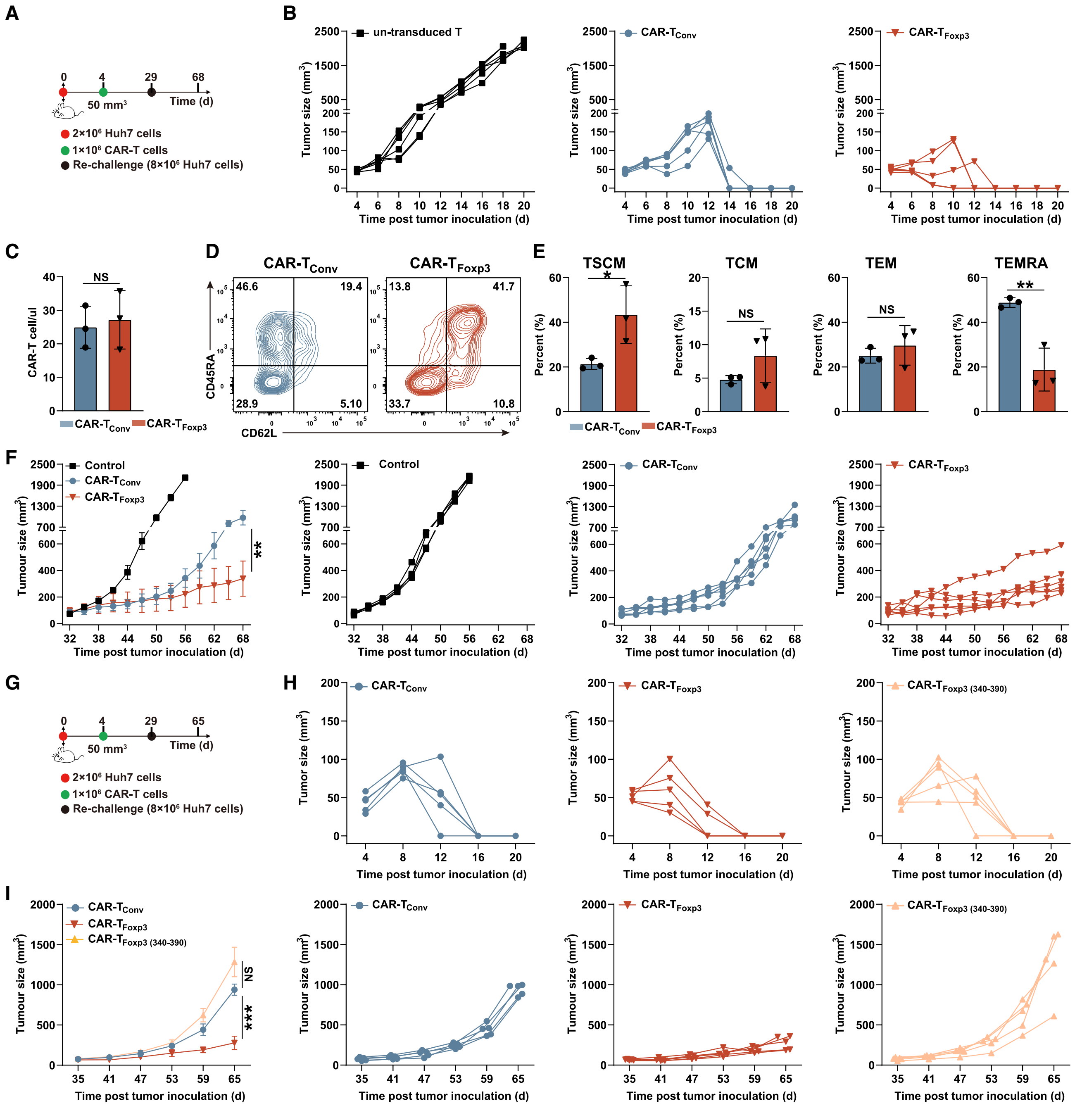

Figure 6. Foxp3 sustains long-lasting antitumor effect and low levels of exhaustion markers in CAR-T$_{Foxp3}$ cells *in vivo*

(A) Experimental timeline of the tumor rechallenge model.

(B) Time-dependent tumor volume changes in the first tumor antigen stimulation (*n* = 6 mice per group).

(C) Quantification of peripheral blood CAR-T cells on day 25.

(D) Representative flow plots of differentiation markers (CD45RA, CD62L) on peripheral blood CAR-T cells after first tumor clearance on day 25 (*n* = 3 biological replicates).

(E) Quantification of (D).

(F) Time-dependent tumor volume changes after tumor rechallenge (control group, *n* = 4 biological replicates; CAR-T$_{Conv}$ group, *n* = 6 biological replicates; CAR-T$_{Foxp3}$ group, *n* = 6 biological replicates).

(G) Experimental timeline of the tumor rechallenge model.

(H) Time-dependent tumor volume changes in the first tumor antigen stimulation (*n* = 5 mice per group).

(I) Time-dependent tumor volume changes after tumor rechallenge (*n* = 5 mice per group).

Data are presented as mean ± SEM (I) or SD (C, E, and F). Statistical significance was calculated using unpaired Student's t tests (C and E) and two-way ANOVA (F and I). NS, not significant, $^*p < 0.05$, $^{**}p < 0.01$, $^{***}p < 0.001$.

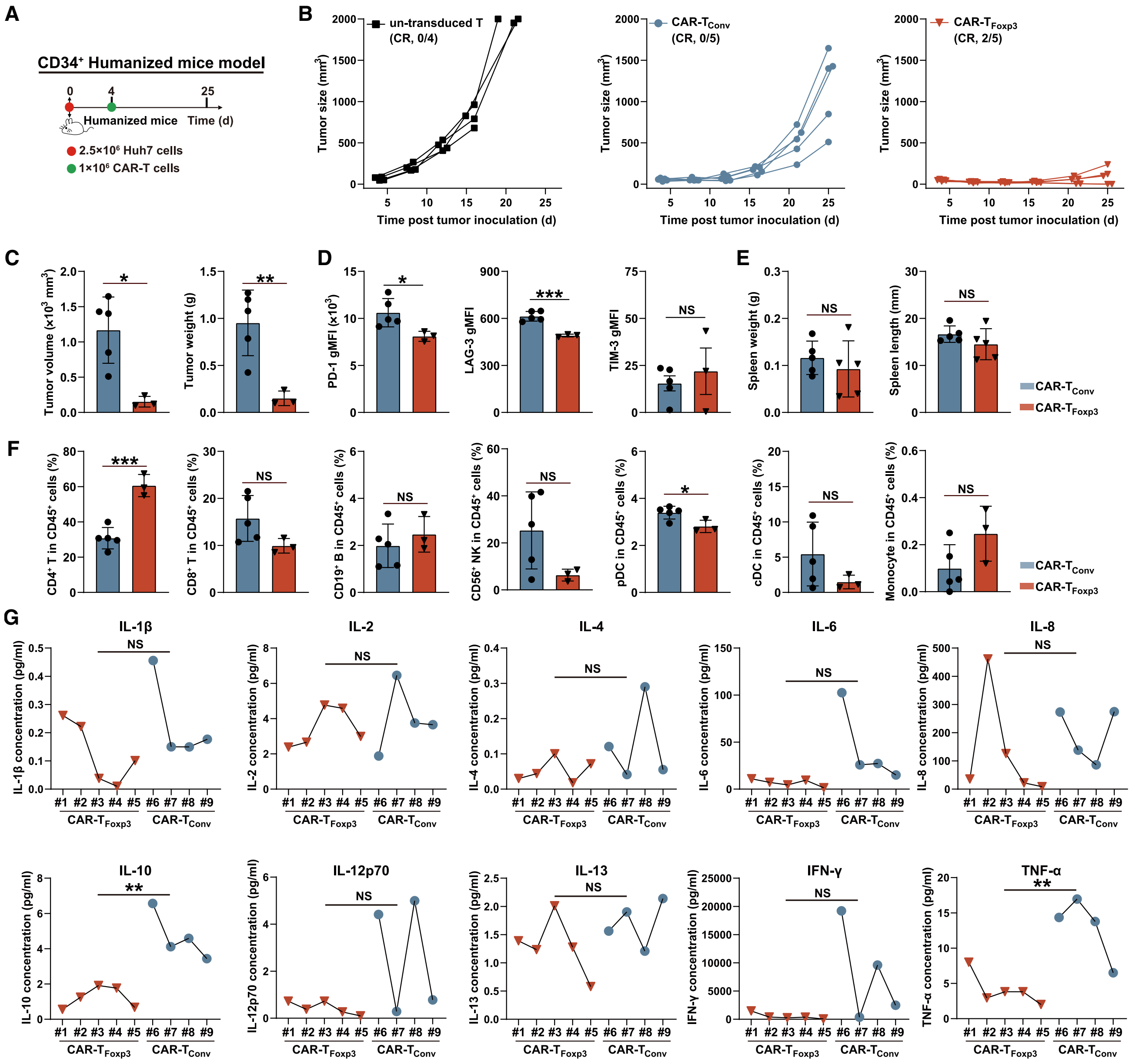

Figure 7. CAR-T$_{Foxp3}$ cells acquire potent antitumor activity but not immune suppression in humanized NSG models

(A) Experimental timeline of humanized NSG model.

(B) Time-dependent tumor volume changes in humanized NSG model (un-transduced T cells, *n* = 4 biological replicates; CAR-T$_{Conv}$ cells, *n* = 5 biological replicates; CAR-T$_{Foxp3}$ cells, *n* = 5 biological replicates).

(C) Quantification of Huh7 tumor volume and tumor weight on day 25 (CAR-T$_{Conv}$ cells, *n* = 5 biological replicates; CAR-T$_{Foxp3}$ cells, *n* = 3 biological replicates).

(D) Quantification of tumor-infiltrating CAR-T cell exhaustion molecules (CAR-T$_{Conv}$ cells, *n* = 5 biological replicates; CAR-T$_{Foxp3}$ cells, *n* = 3 biological replicates).

(E) Quantification of spleen weight and spleen length (CAR-T$_{Conv}$ cells, *n* = 5 biological replicates; CAR-T$_{Foxp3}$ cells, *n* = 5 biological replicates).

(F) Quantification of tumor-infiltrating immune cell compositions (CAR-T$_{Conv}$ cells, *n* = 5 biological replicates; CAR-T$_{Foxp3}$ cells, *n* = 3 biological replicates).

(G) Statistical analysis of peripheral blood human cytokine concentrations (CAR-T$_{Conv}$ cells, *n* = 4 biological replicates; CAR-T$_{Foxp3}$ cells, *n* = 5 biological replicates).

Data are presented showing all individual data points (G) or mean ± SD (C–F). Statistical significance was calculated using unpaired Student's t tests (C–G). NS, not significant, *$p < 0.05$, **$p < 0.01$, ***$p < 0.001$.

In addition, our *in vitro* and *in vivo* functional experiments excluded the suppressive effect of CAR-T$_{Foxp3}$ cells. The expression of Treg inhibitory function-associated genes requires not only transcription factors but also core histone acetylation, which opens chromatin structures and allows transcription factor binding. Foxp3 alone may not be sufficient to regulate the complete Treg transcriptome because it directly binds only around 10% of the genes responsible for Treg inhibitory activity.[50] However, chromatin opening of some metabolism-related genes was increased in CAR-T$_{\text{Foxp3}}$ cells. Meanwhile, CAR-T$_{\text{Foxp3}}$ cells displayed an increased level of lipid metabolism but a lower level of glycolysis and OXPHOS, which helped CAR-T$_{\text{Foxp3}}$ cells to better adapt to the hypoxic TME and suppressed exhaustion-associated inhibitory molecules.

How Foxp3 affects Treg metabolism regulation is debatable. In *Foxp3*-deficient mice, dysregulation of mTORC2 signaling augments aerobic glycolysis and OXPHOS.[14] TGF-β-polarized Tregs increase mitochondrial respiration, and Foxp3 suppresses c-Myc signaling, which represses glycolysis and glutaminolysis.[23] In addition, Foxp3 could prevent fatty acid-induced apoptosis by enhancing fatty acid metabolic pathways in T cells.[24] This disparity might be explained by variances in polarization methods and cell origin. In this study, Foxp3 could shuttle into the cytoplasm and interact with Drp1, which suggested the direct control of mitochondrial metabolism by Foxp3. Drp1, an essential protein for mitochondrial dynamics, regulates mitochondrial fission. Both Ser616 (S616), which initiates mitochondrial fission, and Ser637 (S637), which inhibits mitochondrial fission, are potential sites of phosphorylation for Drp1.[31,32] After antigen stimulation, the activation of mitogen-activated protein kinases (MAPKs) and elevation of ERK phosphorylation led to Drp1 phosphorylation at S616, which initiates mitochondrial fission and promotes aerobic glycolysis and OXPHOS.[33] Based on the predicted Foxp3 and Drp1 interaction sites and our functional experiments, we found that the fragments 600–620 of Drp1 involved in the interaction of Foxp3 and Drp1, which may explain the decrease in Drp1 phosphorylation only at serine 616 by Foxp3; however, further research is required to determine the fundamental mechanisms.

In summary, we demonstrated that Foxp3 remodeled CAR-T cell metabolism to suppress glycolysis and OXPHOS and increase lipid metabolism. The novel CAR-T$_{\text{Foxp3}}$ cells exhibited substantial antitumor efficacy against solid tumors in a human tumor xenograft model and a humanized immune system model, which was attributed to Foxp3-mediated metabolism. Overall, our research emphasizes the prospect of Foxp3-reprogramming metabolism to improve antitumor efficacy of CAR-T cells and may have important implications for clinical immunotherapy. However, the efficacy and persistence of CAR-T$_{\text{Foxp3}}$ cells need to be investigated further in a clinical trial.

Limitations of the study

Herein, we demonstrated that Foxp3 overexpression reprograms CAR-T$_{\text{Foxp3}}$ cell metabolism via cytoplasmic Foxp3-Drp1 interaction. However, the precise mechanism by which Foxp3 specifically reduces Drp1 phosphorylation exclusively at serine 616 remains to be elucidated. Notably, unlike natural regulatory Tregs, Foxp3 overexpression does not confer immunosuppressive capacity to CAR-T$_{\text{Foxp3}}$ cells. This functional discrepancy could potentially be attributed to fundamental differences in chromatin accessibility patterns and inhibitory molecule expression profiles between CAR-T$_{\text{Foxp3}}$ cells and natural Tregs, though the underlying regulatory mechanisms governing these distinctions warrant systematic exploration. Finally, while Foxp3 in CAR-T$_{\text{Foxp3}}$ cells is primarily localized in the cytoplasm with detectable nuclear expression, the functional relevance of nuclear Foxp3, particularly its potential role in transcriptional regulation, remains undefined.

RESOURCE AVAILABILITY

Lead contact

Further information and requests for resources and reagents should be directed to the lead contact, Feifei Luo (feifeiluo@fudan.edu.cn).

Materials availability

Plasmids generated in this paper can be requested directly from the lead contact.

Data and code availability

The RNA-seq and ATAC-seq raw data have been deposited in the Genome Sequence Archive in the National Genomics Data Center, the China National Center for Bioinformation/Beijing Institute of Genomics, and the Chinese Academy of Sciences (GSA database: HRA005801), which are publicly accessible at https://ngdc.cncb.ac.cn/gsa-human. The raw data of [U-C13]-glucose and [U-C13]-glutamine metabolism, non-targeted lipidomics, and non-targeted mass spectrometry have been deposited into the China National GeneBank (CNGB) with accession number CNP0007043. Source data for graphs and uncropped western blot scans are provided in Data S1.

ACKNOWLEDGMENTS

We thank Prof. Shimin Zhao (Fudan University) and Prof. Bin Li (Shanghai Jiao Tong University) for critical guidance and review of the paper. This study was supported by the National Natural Science Foundation of China (no. 82121002, 82130050, and 82330053), the National Program for Support of Top-notch Young Professionals of China (to F.L.), and the Shenzhen Institute of Synthetic Biology Scientific Research Program (no. ZTXM20214002).

AUTHOR CONTRIBUTIONS

F.L. and Y.C. designed and supervised the research. C.N. and H.W. carried out the majority of experiments and analyzed bioinformatics data. H.W. undertook and analyzed ATAC-seq experiments. C.N., X.P., Y.W., and H.S. designed the graphical abstract and conducted statistical analysis. J. Qie, C.L., W.Z., S.M., and J. Qian. performed the non-targeted mass spectrometry experiment and analyzed data. F.L., C.N., Y.C., K.Z., and X.P. wrote the manuscript. J.L., W.T., D.Z., H.Y., R.L., L.W., Z.L., and Y.G. revised and edited the paper.

DECLARATION OF INTERESTS

Fudan University is in the process of applying for a patent application covering the preparation method and function of CAR-T$_{\text{Foxp3}}$ cells that lists Y.C., C.N., and F.L. as inventors.

STAR★METHODS

Detailed methods are provided in the online version of this paper and include the following:

- KEY RESOURCES TABLE
- EXPERIMENTAL MODEL AND STUDY PARTICIPANT DETAILS
  - Cell lines
  - Primary cell culture
  - Animals
- METHOD DETAILS
  - Generation of CAR-T cells
  - Staining and flow cytometry
  - ECAR and OCR measurements
  - Non-targeted mass spectrometry and analysis
  - [U-C13]-Glucose and [U-C13]-glutamine metabolism
  - RNA extraction and RNA-seq
  - BiFC assay
  - GST pull-down assays
  - Protein interaction analysis
  - Live cell imaging for cytotoxicity assay
  - ATAC-seq and data processing

  - ○ T cell proliferation suppression assay
  - ○ Illustration tool
- QUANTIFICATION AND STATISTICAL ANALYSIS

SUPPLEMENTAL INFORMATION

Supplemental information can be found online at https://doi.org/10.1016/j.cmet.2025.04.008.

Received: November 21, 2023
Revised: October 14, 2024
Accepted: April 14, 2025
Published: May 5, 2025

REFERENCES

1. Maude, S.L., Frey, N., Shaw, P.A., Aplenc, R., Barrett, D.M., Bunin, N.J., Chew, A., Gonzalez, V.E., Zheng, Z., Lacey, S.F., et al. (2014). Chimeric antigen receptor T cells for sustained remissions in leukemia. N. Engl. J. Med. *371*, 1507–1517. https://doi.org/10.1056/NEJMoa1407222.
2. Neelapu, S.S., Locke, F.L., Bartlett, N.L., Lekakis, L.J., Miklos, D.B., Jacobson, C.A., Braunschweig, I., Oluwole, O.O., Siddiqi, T., Lin, Y., et al. (2017). Axicabtagene ciloleucel CAR T-cell therapy in refractory large B-cell lymphoma. N. Engl. J. Med. *377*, 2531–2544. https://doi.org/10.1056/NEJMoa1707447.
3. Park, J.H., Rivière, I., Gonen, M., Wang, X., Sénéchal, B., Curran, K.J., Sauter, C., Wang, Y., Santomasso, B., Mead, E., et al. (2018). Long-term follow-up of CD19 CAR therapy in acute lymphoblastic leukemia. N. Engl. J. Med. *378*, 449–459. https://doi.org/10.1056/NEJMoa1709919.
4. Lamers, C.H.J., Sleijfer, S., Vulto, A.G., Kruit, W.H.J., Kliffen, M., Debets, R., Gratama, J.W., Stoter, G., and Oosterwijk, E. (2006). Treatment of metastatic renal cell carcinoma with autologous T-lymphocytes genetically retargeted against carbonic anhydrase IX: first clinical experience. J. Clin. Oncol. *24*, e20–e22. https://doi.org/10.1200/JCO.2006.05.9964.
5. Ahmed, N., Brawley, V.S., Hegde, M., Robertson, C., Ghazi, A., Gerken, C., Liu, E., Dakhova, O., Ashoori, A., Corder, A., et al. (2015). Human epidermal growth factor receptor 2 (HER2) -specific chimeric antigen receptor-modified T cells for the immunotherapy of HER2-positive sarcoma. J. Clin. Oncol. *33*, 1688–1696. https://doi.org/10.1200/JCO.2014.58.0225.
6. Scharping, N.E., Menk, A.V., Moreci, R.S., Whetstone, R.D., Dadey, R.E., Watkins, S.C., Ferris, R.L., and Delgoffe, G.M. (2016). The tumor microenvironment represses T cell mitochondrial biogenesis to drive intratumoral T cell metabolic insufficiency and dysfunction. Immunity *45*, 374–388. https://doi.org/10.1016/j.immuni.2016.07.009.
7. Peng, J.J., Wang, L., Li, Z., Ku, C.L., and Ho, P.C. (2023). Metabolic challenges and interventions in CAR T cell therapy. Sci. Immunol. *8*, eabq3016. https://doi.org/10.1126/sciimmunol.abq3016.
8. Zhang, S., Zhang, X., Wang, K., Xu, X., Li, M., Zhang, J., Zhang, Y., Hao, J., Sun, X., Chen, Y., et al. (2018). Newly generated CD4(+) T cells acquire metabolic quiescence after thymic egress. J. Immunol. *200*, 1064–1077. https://doi.org/10.4049/jimmunol.1700721.
9. Chapman, N.M., Boothby, M.R., and Chi, H. (2020). Metabolic coordination of T cell quiescence and activation. Nat. Rev. Immunol. *20*, 55–70. https://doi.org/10.1038/s41577-019-0203-y.
10. Wang, R., Dillon, C.P., Shi, L.Z., Milasta, S., Carter, R., Finkelstein, D., McCormick, L.L., Fitzgerald, P., Chi, H., Munger, J., et al. (2011). The transcription factor Myc controls metabolic reprogramming upon T lymphocyte activation. Immunity *35*, 871–882. https://doi.org/10.1016/j.immuni.2011.09.021.
11. Yang, K., Shrestha, S., Zeng, H., Karmaus, P.W.F., Neale, G., Vogel, P., Guertin, D.A., Lamb, R.F., and Chi, H. (2013). T cell exit from quiescence and differentiation into Th2 cells depend on Raptor-mTORC1-mediated metabolic reprogramming. Immunity *39*, 1043–1056. https://doi.org/10.1016/j.immuni.2013.09.015.
12. Buck, M.D., Sowell, R.T., Kaech, S.M., and Pearce, E.L. (2017). Metabolic instruction of immunity. Cell *169*, 570–586. https://doi.org/10.1016/j.cell.2017.04.004.
13. Priyadharshini, B., Loschi, M., Newton, R.H., Zhang, J.W., Finn, K.K., Gerriets, V.A., Huynh, A., Rathmell, J.C., Blazar, B.R., and Turka, L.A. (2018). Cutting edge: TGF-β and phosphatidylinositol 3-kinase signals modulate distinct metabolism of regulatory T cell subsets. J. Immunol. *201*, 2215–2219. https://doi.org/10.4049/jimmunol.1800311.
14. Charbonnier, L.M., Cui, Y., Stephen-Victor, E., Harb, H., Lopez, D., Bleesing, J.J., Garcia-Lloret, M.I., Chen, K., Ozen, A., Carmeliet, P., et al. (2019). Functional reprogramming of regulatory T cells in the absence of Foxp3. Nat. Immunol. *20*, 1208–1219. https://doi.org/10.1038/s41590-019-0442-x.
15. Matias, M.I., Yong, C.S., Foroushani, A., Goldsmith, C., Mongellaz, C., Sezgin, E., Levental, K.R., Talebi, A., Perrault, J., Rivière, A., et al. (2021). Regulatory T cell differentiation is controlled by αKG-induced alterations in mitochondrial metabolism and lipid homeostasis. Cell Rep. *37*, 109911. https://doi.org/10.1016/j.celrep.2021.109911.
16. Macintyre, A.N., Gerriets, V.A., Nichols, A.G., Michalek, R.D., Rudolph, M.C., Deoliveira, D., Anderson, S.M., Abel, E.D., Chen, B.J., Hale, L.P., et al. (2014). The glucose transporter Glut1 is selectively essential for CD4 T cell activation and effector function. Cell Metab. *20*, 61–72. https://doi.org/10.1016/j.cmet.2014.05.004.
17. Beier, U.H., Angelin, A., Akimova, T., Wang, L., Liu, Y., Xiao, H., Koike, M.A., Hancock, S.A., Bhatti, T.R., Han, R., et al. (2015). Essential role of mitochondrial energy metabolism in Foxp3$^+$ T-regulatory cell function and allograft survival. FASEB J. *29*, 2315–2326. https://doi.org/10.1096/fj.14-268409.
18. Gerriets, V.A., Kishton, R.J., Nichols, A.G., Macintyre, A.N., Inoue, M., Ilkayeva, O., Winter, P.S., Liu, X., Priyadharshini, B., Slawinska, M.E., et al. (2015). Metabolic programming and PDHK1 control CD4+ T cell subsets and inflammation. J. Clin. Invest. *125*, 194–207. https://doi.org/10.1172/JCI76012.
19. Pacella, I., Procaccini, C., Focaccetti, C., Miacci, S., Timperi, E., Faicchia, D., Severa, M., Rizzo, F., Coccia, E.M., Bonacina, F., et al. (2018). Fatty acid metabolism complements glycolysis in the selective regulatory T cell expansion during tumor growth. Proc. Natl. Acad. Sci. USA. *115*, E6546–E6555. https://doi.org/10.1073/pnas.1720113115.
20. Kumagai, S., Togashi, Y., Sakai, C., Kawazoe, A., Kawazu, M., Ueno, T., Sato, E., Kuwata, T., Kinoshita, T., Yamamoto, M., et al. (2020). An oncogenic alteration creates a microenvironment that promotes tumor progression by conferring a metabolic advantage to regulatory T cells. Immunity *53*, 187–203.e8. https://doi.org/10.1016/j.immuni.2020.06.016.
21. Wang, H., Franco, F., Tsui, Y.C., Xie, X., Trefny, M.P., Zappasodi, R., Mohmood, S.R., Fernández-García, J., Tsai, C.H., Schulze, I., et al. (2020). CD36-mediated metabolic adaptation supports regulatory T cell survival and function in tumors. Nat. Immunol. *21*, 298–308. https://doi.org/10.1038/s41590-019-0589-5.
22. Watson, M.J., Vignali, P.D.A., Mullett, S.J., Overacre-Delgoffe, A.E., Peralta, R.M., Grebinoski, S., Menk, A.V., Rittenhouse, N.L., DePeaux, K., Whetstone, R.D., et al. (2021). Metabolic support of tumour-infiltrating regulatory T cells by lactic acid. Nature *591*, 645–651. https://doi.org/10.1038/s41586-020-03045-2.
23. Angelin, A., Gil-de-Gómez, L., Dahiya, S., Jiao, J., Guo, L., Levine, M.H., Wang, Z., Quinn, W.J., 3rd, Kopinski, P.K., Wang, L., et al. (2017). Foxp3 reprograms T cell metabolism to function in low-glucose, high-lactate environments. Cell Metab. *25*, 1282–1293.e7. https://doi.org/10.1016/j.cmet.2016.12.018.
24. Howie, D., Cobbold, S.P., Adams, E., Ten Bokum, A., Necula, A.S., Zhang, W., Huang, H., Roberts, D.J., Thomas, B., Hester, S.S., et al. (2017). Foxp3 drives oxidative phosphorylation and protection from lipotoxicity. JCI Insight *2*, e89160. https://doi.org/10.1172/jci.insight.89160.
25. Ramos, C.A., Rouce, R., Robertson, C.S., Reyna, A., Narala, N., Vyas, G., Mehta, B., Zhang, H., Dakhova, O., Carrum, G., et al. (2018). In Vivo Fate and Activity of Second- versus Third-Generation CD19-Specific CAR-T

Cells in B Cell Non-Hodgkin's Lymphomas. Mol. Ther. *26*, 2727–2737. https://doi.org/10.1016/j.ymthe.2018.09.009.

26. Ruggieri, V., Agriesti, F., Scrima, R., Laurenzana, I., Perrone, D., Tataranni, T., Mazzoccoli, C., Lo Muzio, L., Capitanio, N., and Piccoli, C. (2015). Dichloroacetate, a selective mitochondria-targeting drug for oral squamous cell carcinoma: a metabolic perspective of treatment. Oncotarget *6*, 1217–1230. https://doi.org/10.18632/oncotarget.2721.
27. Zhou, L., Liu, L., Chai, W., Zhao, T., Jin, X., Guo, X., Han, L., and Yuan, C. (2019). Dichloroacetic acid upregulates apoptosis of ovarian cancer cells by regulating mitochondrial function. OncoTargets Ther. *12*, 1729–1739. https://doi.org/10.2147/OTT.S194329.
28. Giacomello, M., Pyakurel, A., Glytsou, C., and Scorrano, L. (2020). The cell biology of mitochondrial membrane dynamics. Nat. Rev. Mol. Cell Biol. *21*, 204–224. https://doi.org/10.1038/s41580-020-0210-7.
29. Xie, J.H., Li, Y.Y., and Jin, J. (2020). The essential functions of mitochondrial dynamics in immune cells. Cell. Mol. Immunol. *17*, 712–721. https://doi.org/10.1038/s41423-020-0480-1.
30. Magg, T., Mannert, J., Ellwart, J.W., Schmid, I., and Albert, M.H. (2012). Subcellular localization of FOXP3 in human regulatory and nonregulatory T cells. Eur. J. Immunol. *42*, 1627–1638. https://doi.org/10.1002/eji.201141838.
31. Cereghetti, G.M., Stangherlin, A., Martins de Brito, O., Chang, C.R., Blackstone, C., Bernardi, P., and Scorrano, L. (2008). Dephosphorylation by calcineurin regulates translocation of Drp1 to mitochondria. Proc. Natl. Acad. Sci. USA. *105*, 15803–15808. https://doi.org/10.1073/pnas.0808249105.
32. Archer, S.L. (2013). Mitochondrial dynamics-mitochondrial fission and fusion in human diseases. N. Engl. J. Med. *369*, 2236–2251. https://doi.org/10.1056/NEJMra1215233.
33. Kashatus, J.A., Nascimento, A., Myers, L.J., Sher, A., Byrne, F.L., Hoehn, K.L., Counter, C.M., and Kashatus, D.F. (2015). Erk2 phosphorylation of Drp1 promotes mitochondrial fission and MAPK-driven tumor growth. Mol. Cell *57*, 537–551. https://doi.org/10.1016/j.molcel.2015.01.002.
34. Xu, C., Fu, Y., Liu, S., Trittipo, J., Lu, X., Qi, R., Du, H., Yan, C., Zhang, C., Wan, J., et al. (2021). BATF regulates T regulatory cell functional specification and fitness of triglyceride metabolism in restraining allergic responses. J. Immunol. *206*, 2088–2100. https://doi.org/10.4049/jimmunol.2001184.
35. Itahashi, K., Irie, T., Yuda, J., Kumagai, S., Tanegashima, T., Lin, Y.T., Watanabe, S., Goto, Y., Suzuki, J., Aokage, K., et al. (2022). BATF epigenetically and transcriptionally controls the activation program of regulatory T cells in human tumors. Sci. Immunol. *7*, eabk0957. https://doi.org/10.1126/sciimmunol.abk0957.
36. Obradovic, A., Ager, C., Turunen, M., Nirschl, T., Khosravi-Maharlooei, M., Iuga, A., Jackson, C.M., Yegnasubramanian, S., Tomassoni, L., Fernandez, E.C., et al. (2023). Systematic elucidation and pharmacological targeting of tumor-infiltrating regulatory T cell master regulators. Cancer Cell *41*, 933–949.e11. https://doi.org/10.1016/j.ccell.2023.04.003.
37. Arts, R.J.W., Novakovic, B., Ter Horst, R., Carvalho, A., Bekkering, S., Lachmandas, E., Rodrigues, F., Silvestre, R., Cheng, S.C., Wang, S.Y., et al. (2016). Glutaminolysis and Fumarate Accumulation Integrate Immunometabolic and Epigenetic Programs in Trained Immunity. Cell Metab. *24*, 807–819. https://doi.org/10.1016/j.cmet.2016.10.008.
38. Noe, J.T., Rendon, B.E., Geller, A.E., Conroy, L.R., Morrissey, S.M., Young, L.E.A., Bruntz, R.C., Kim, E.J., Wise-Mitchell, A., Barbosa de Souza Rizzo, M., et al. (2021). Lactate supports a metabolic-epigenetic link in macrophage polarization. Sci. Adv. *7*, eabi8602. https://doi.org/10.1126/sciadv.abi8602.
39. Li, W., Kou, J., Qin, J., Li, L., Zhang, Z., Pan, Y., Xue, Y., and Du, W. (2021). NADPH levels affect cellular epigenetic state by inhibiting HDAC3-Ncor complex. Nat. Metab. *3*, 75–89. https://doi.org/10.1038/s42255-020-00330-2.
40. Zheng, Y., Josefowicz, S.Z., Kas, A., Chu, T.T., Gavin, M.A., and Rudensky, A.Y. (2007). Genome-wide analysis of Foxp3 target genes in developing and mature regulatory T cells. Nature *445*, 936–940. https://doi.org/10.1038/nature05563.
41. Tanaka, A., and Sakaguchi, S. (2017). Regulatory T cells in cancer immunotherapy. Cell Res. *27*, 109–118. https://doi.org/10.1038/cr.2016.151.
42. Togashi, Y., Shitara, K., and Nishikawa, H. (2019). Regulatory T cells in cancer immunosuppression - implications for anticancer therapy. Nat. Rev. Clin. Oncol. *16*, 356–371. https://doi.org/10.1038/s41571-019-0175-7.
43. Miska, J., Lee-Chang, C., Rashidi, A., Muroski, M.E., Chang, A.L., Lopez-Rosas, A., Zhang, P., Panek, W.K., Cordero, A., Han, Y., et al. (2019). HIF-1α is a metabolic switch between glycolytic-driven migration and oxidative phosphorylation-driven immunosuppression of Tregs in glioblastoma. Cell Rep. *27*, 226–237.e4. https://doi.org/10.1016/j.celrep.2019.03.029.
44. Kawalekar, O.U., O'Connor, R.S., Fraietta, J.A., Guo, L., McGettigan, S.E., Posey, A.D., Jr., Patel, P.R., Guedan, S., Scholler, J., Keith, B., et al. (2016). Distinct Signaling of Coreceptors Regulates Specific Metabolism Pathways and Impacts Memory Development in CAR T Cells. Immunity *44*, 380–390. https://doi.org/10.1016/j.immuni.2016.01.021.
45. Menk, A.V., Scharping, N.E., Rivadeneira, D.B., Calderon, M.J., Watson, M.J., Dunstane, D., Watkins, S.C., and Delgoffe, G.M. (2018). 4–1BB costimulation induces T cell mitochondrial function and biogenesis enabling cancer immunotherapeutic responses. J. Exp. Med. *215*, 1091–1100. https://doi.org/10.1084/jem.20171068.
46. Cappell, K.M., and Kochenderfer, J.N. (2021). A comparison of chimeric antigen receptors containing CD28 versus 4–1BB costimulatory domains. Nat. Rev. Clin. Oncol. *18*, 715–727. https://doi.org/10.1038/s41571-021-00530-z.
47. Field, C.S., Baixauli, F., Kyle, R.L., Puleston, D.J., Cameron, A.M., Sanin, D.E., Hippen, K.L., Loschi, M., Thangavelu, G., Corrado, M., et al. (2020). Mitochondrial integrity regulated by lipid metabolism is a cell-intrinsic checkpoint for Treg suppressive function. Cell Metab. *31*, 422–437.e5. https://doi.org/10.1016/j.cmet.2019.11.021.
48. Williams, L.M., and Rudensky, A.Y. (2007). Maintenance of the Foxp3-dependent developmental program in mature regulatory T cells requires continued expression of Foxp3. Nat. Immunol. *8*, 277–284. https://doi.org/10.1038/ni1437.
49. van der Vliet, H.J.J., and Nieuwenhuis, E.E. (2007). IPEX as a result of mutations in FOXP3. Clin. Dev. Immunol. *2007*, 89017. https://doi.org/10.1155/2007/89017.
50. Trujillo-Ochoa, J.L., Kazemian, M., and Afzali, B. (2023). The role of transcription factors in shaping regulatory T cell identity. Nat. Rev. Immunol. *23*, 842–856. https://doi.org/10.1038/s41577-023-00893-7.

STAR★METHODS

KEY RESOURCES TABLE

REAGENT or RESOURCE	SOURCE	IDENTIFIER
Antibodies		
Ultra-LEAF™ Purified anti-human CD3 Antibody	BioLegend	Cat#300437; RRID: AB_11147760
Ultra-LEAF™ Purified anti-human CD28 Antibody	BioLegend	Cat#377803; RRID: AB_2910434
PE/Cyanine7 anti-human CD279 (PD-1) Antibody	BioLegend	Cat#329918; RRID: AB_2159324
PerCP/Cyanine5.5 anti-human CD223 (LAG-3) Antibody	BioLegend	Cat#369312; RRID: AB_2629755
Brilliant Violet 421™ anti-human CD366 (TIM-3) Antibody	BioLegend	Cat#345008; RRID: AB_11218598
APC/Fire 750 anti-human CD28 Antibody	BioLegend	Cat#302951; RRID: AB_2617038
PE/Cyanine5 anti-human CD45RA Antibody	BioLegend	Cat#304110; RRID: AB_314414
APC/Fire 810 anti-human CD62L Antibody	BioLegend	Cat#304865; RRID: AB_2894453
Alexa Fluor 700 anti-human CD95 (Fas) Antibody	BioLegend	Cat#305647; RRID: AB_2750144
PerCP anti-human CD197 (CCR7) Antibody	BioLegend	Cat#353241; RRID: AB_2564545
PE anti-human TCF1 (TCF7) Antibody	BioLegend	Cat#655208; RRID: AB_2728492
PE anti-human IFN-γ Antibody	BioLegend	Cat#502509; RRID: AB_315234
PE/Cyanine7 anti-human TNF-α Antibody	BioLegend	Cat#502930; RRID: AB_2204079
PE/Cyanine7 anti-human/mouse Granzyme B Recombinant Antibody	BioLegend	Cat#372214; RRID: AB_2728381
Alexa Fluor® 647 anti-mouse/rat/human FOXP3 Antibody	BioLegend	Cat#320014; RRID: AB_439750
PerCP-eFluor 710 anti-human CD27 Monoclonal Antibody	EBioscience	Cat#46-0271-80; RRID: AB_1834448
eFluor 450 anti-human CD69 Monoclonal Antibody	EBioscience	Cat#48-0699-41; RRID: AB_2574024
eFluor 660 anti-human EOMES Monoclonal Antibody	EBioscience	Cat#50-4877-41; RRID: AB_2574228
Anti-human CD3 Monoclonal Antibody	EBioscience	Cat#14-0038-82; RRID: AB_467059
APC/Cyanine7 anti-human CD303 (BDCA-2) Antibody	BioLegend	Cat#354238; RRID: AB_2800951
PE anti-human CD45 Antibody	BioLegend	Cat#304058; RRID: AB_2564156
APC anti-human HLA-DR Antibody	BioLegend	Cat#307610; RRID: AB_314688
Brilliant Violet 570™ anti-human CD4 Antibody	BioLegend	Cat#317445; RRID: AB_2561582
Brilliant Violet 785™ anti-human CD19 Antibody	BioLegend	Cat#302240; RRID: AB_2563442
Brilliant Violet 605™ anti-human CD14 Antibody	BioLegend	Cat#325640; RRID: AB_3097607
PE/Cyanine7 anti-human CD11c Antibody	BioLegend	Cat#301608; RRID: AB_389351
Brilliant Violet 650™ anti-human CD3 Antibody	BioLegend	Cat#317324; RRID: AB_2563352
PE anti-human CD72 Antibody	BioLegend	Cat#316208; RRID: AB_2819946
PE/Cyanine7 anti-human CD127 (IL-7Rα) Antibody	BioLegend	Cat#351320; RRID: AB_10897098
APC/Cyanine7 anti-human CD25 Antibody	BioLegend	Cat#302614; RRID: AB_314284

(*Continued on next page*)

Continued

REAGENT or RESOURCE	SOURCE	IDENTIFIER
PE/Cyanine7 anti-human IL-2 Antibody	BioLegend	Cat#500326; RRID: AB_2125593
Brilliant Violet 421™ anti-human CD39 Antibody	BioLegend	Cat#328214; RRID: AB_2564575
PerCP/Cyanine5.5 anti-human CD152 (CTLA-4) Antibody	BioLegend	Cat#369608; RRID: AB_2629674
GST Tag Monoclonal Antibody	Proteintech	Cat#66001-2-Ig; RRID: AB_2881488
6*His, His-Tag Monoclonal Antibody	Proteintech	Cat#66005-1-Ig; RRID: AB_11232599
Anti-human PD-1 Antibody	Cell Signaling Technology	Cat#86163T; RRID: AB_2728833
DRP1 (D6C7) Rabbit mAb	Cell Signaling Technology	Cat#8570S; RRID: AB_10950498
Phospho-DRP1 (Ser616) Antibody	Cell Signaling Technology	Cat#3455S; RRID: AB_2085352
Alexa Fluor 647 Goat Anti-Human IgG,F(ab′) 2 fragment specific	Jackson ImmunoResearch	Cat#109-605-006; RRID: AB_2337881
Foxp3 Monoclonal Antibody (FJK-16s)	Thermo Fisher Scientific	Cat#14-5773-82; RRID: AB_467576
Phospho-DRP1(Ser637) Polyclonal Antibody	Thermo Fisher Scientific	Cat#PA5-101038; RRID: AB_2815867
Anti-CDK1 Antibody	Abcam	Cat#ab32094; RRID: AB_726757
Anti-beta Actin Monoclonal Antibody	Thermo Fisher Scientific	Cat# AM4302; RRID: AB_2536382
ERK1/ERK2 Monoclonal Antibody (ERK-7D8)	Thermo Fisher Scientific	Cat#13-6200; RRID: AB_2533024
Phospho-ERK1/2 (Thr202, Tyr204) Monoclonal Antibody	Thermo Fisher Scientific	Cat#14-9109-82; RRID: AB_2572926
Biological samples		
Human peripheral blood mononuclear cells	Oribiotech (Shanghai, China)	N/A
Chemicals, peptides, and recombinant proteins		
XF 1.0 M Glucose Solution	Agilent	Cat#103577-100
XF 100 mM Pyruvate Solution	Agilent	Cat#103578-100
XF 200 mM Glutamine Solution	Agilent	Cat#103579-100
XF RPMI Base Medium (pH 7.4)	Agilent	Cat#103576-100
Seahorse XFe96/XF Pro FluxPak Mini	Agilent	Cat#103793-100
Sodium Pyruvate (100 mM)	Thermo Fisher	Cat#11360070
Non-Essential Amino Acids Solution	Thermo Fisher	Cat#11140050
HEPES (1 M)	Thermo Fisher	Cat#15630080
GlutaMAX	Thermo Fisher	Cat#35050061
TRIzol	Thermo Fisher	Cat#15596026
Sodium Dichloroacetate	MedChemExpress	Cat#HY-Y0445A
L-Glutamine (U-13C5, 98.0%)	MedChemExpress	Cat#HY-N0390S1
Bodipy 493/503	MedChemExpress	Cat#HY-W090090
Cell Proliferation Dye eFluor™ 670	EBioscience	Cat#65-0840-85
Foxp3/Transcription Factor Staining Buffer Set	EBioscience	Cat#00-5523-00
Methanol (HPLC)	Honeywell	Cat#AH230-4HC
Acetonitrile (HPLC)	Honeywell	Cat#AH015-4LT
Mito-Tracker Green	Beyotime (Shanghai, China)	Cat#C1048
Triton X-100 Solution (10%, Sterile)	Beyotime (Shanghai, China)	Cat#ST797-100ml
D-Glucose (U-13C6, 99%)	Cambridge Isotope Laboratories	Cat#CLM-1396-PK
Recombinant Human IL-2 Protein	R&D Systems	Cat#202-IL-500
JC-1	GlpBio	Cat#GC12331
RetroNectin	TAKARA	Cat#T100A

(*Continued on next page*)

Continued

REAGENT or RESOURCE	SOURCE	IDENTIFIER
Polyethylenimine Hydrochloride (MW 40,000)	Polysciences	Cat#24765-1
Water (HPLC)	Fisher	Cat#7732-18-5
Critical commercial assays		
CD4$^+$CD25$^+$ Regulatory T Cell Isolation Kit, human	Miltenyi Biotec	Cat#130-091-301
Pan T cell Isolation Kit, human	Miltenyi Biotec	Cat#130-096-535
XF Glycolysis Stress Test Kit	Agilent	Cat#103020-100
XF Cell Mito Stress Test Kit	Agilent	Cat#103015-100
HiSpeed Plasmid Midi Kit	QIAGEN	Cat#12643
QIAquick PCR Purification Kit	QIAGEN	Cat#28104
Zombie Yellow™ Fixable Viability Kit	BioLegend	Cat#423103
FITC Annexin V Apoptosis Detection Kit with 7-AAD	BioLegend	Cat#640922
LIVE/DEAD Fixable Aqua Dead Cell Stain Kit	Thermo Fisher	Cat#L34957
One step PCR Cloning Kit	Novoprotein (Suzhou, China)	Cat#NR005-01A
Hieff NGS® MaxUp II Dual-mode mRNA Library Prep Kit for Illumina	Yeasen (Shanghai, China)	Cat#12300ES96
Deposited data		
Raw data: RNA-seq and ATAC-seq	This paper	GSA database: HRA005801
Raw data: [U-C13]-Glucose and [U-C13]-glutamine metabolism, non-targeted lipidomics, and non-targeted mass spectrometry	This paper	CNGB database: CNP0007043
Uncropped western blots and Raw data used to generate figures	This paper	Data S1
Experimental models: Cell lines		
HEK293T	Cell Bank of Chinese Academy of Sciences	Cat#SCSP-502
Huh7	Cell Bank of Chinese Academy of Sciences	Cat#SCSP-526
Experimental models: Organisms/strains		
Mouse: NOD.Cg-Prkdc^{scid}Il2rg^{em1Smoc}	Shanghai Model Organisms Center (Shanghai, China)	NM-NSG-001
Recombinant DNA		
pWPT-EF1α-GPC3(HU9F2)-CAR	This paper	N/A
pWPT-EF1α-GPC3(HU9F2)-CAR-T2A-Foxp3	This paper	N/A
pBiFC-CMV-Opa1-VN173	This paper	N/A
pBiFC-CMV-Mfn1-VN173	This paper	N/A
pBiFC-CMV-Mfn1-VN173	This paper	N/A
pBiFC-CMV-Drp1-VN173	This paper	N/A
pBiFC-CMV-Foxp3-VC155	This paper	N/A
pEGFP-CMV-Neongreen-linker-Foxp3	This paper	N/A
pEGFP-CMV-mCherry-linker-Drp1	This paper	N/A
PCDH-CMV-Foxp3-6*His	This paper	N/A
PCDH-CMV-GST	This paper	N/A
PCDH-CMV-GST-Drp1	This paper	N/A

(*Continued on next page*)

Continued

REAGENT or RESOURCE	SOURCE	IDENTIFIER
Software and algorithms		
SAMBAMBA	A. Tarasov, A.J. Vilella, E. Cuppen	GitHub – biod/sambamba: Tools for working with SAM/BAM data
FlowJo v10	FlowJo, LLC	https://www.flowjo.com
GraphPad Prism v8.0	GraphPad	https://www.graphpad.com
Wave	Agilent	https://www.agilent.com/en/product/cell-analysis/real-time-cell-metabolic-analysis/xf-software/seahorse-wave-desktop-software-740897
FastQC	Simon Andrews	https://www.bioinformatics.babraham.ac.uk/projects/fastqc/
MultiQC	Philip Ewels	https://multiqc.info/
Trim Galore	Felix Krueger	https://www.bioinformatics.babraham.ac.uk/projects/trim_galore/
HISAT2	Daehwan Kim	http://daehwankimlab.github.io/hisat2/
Subread	Yang Liao	https://subread.sourceforge.net/
Samtools	Heng Li, Bob Handsaker	https://github.com/samtools/samtools
deepTools	Ramírez, Fidel	https://deeptools.readthedocs.io/en/develop/
Limma	Matthew E. Ritchie	http://bioconductor.org/packages/release/bioc/html/limma.html
Bowtie2	Langmead B, Salzberg S	Bowtie 2: fast and sensitive read alignment (sourceforge.net)
GSEA	Aravind Subramanian	https://www.gsea-msigdb.org/gsea/index.jsp
Gene Ontology Resource	Open Biological Ontologies Foundry	http://geneontology.org/
The Integrative Genome Viewer (IGV)	Broad Institute	https://github.com/igvteam/igv
pheatmap	Raivo Kolde	https://www.rdocumentation.org/packages/pheatmap/versions/1.0.12/topics/pheatmap
clusterProfiler	Guangchuang Yu	https://bioconductor.org/packages/release/bioc/html/clusterProfiler.html
ChIPseeker	Wang Q, Li M	https://bioconductor.org/packages/release/bioc/html/ChIPseeker.html
MACS2	Tao Liu	https://pypi.org/project/MACS2/
Bedtools	Quinlan AR and Hall IM	bedtools: a powerful toolset for genome arithmetic — bedtools 2.31.0 documentation
Homer	cbenner@ucsd.edu	http://homer.ucsd.edu/homer/motif/
BioRender	BioRender Software	https://www.biorender.com/
Other		
RPMI 1640 medium, no glucose	Thermo Fisher	Cat#11879020
RPMI 1640 medium, no glutamine	Thermo Fisher	Cat#21870076
DMEM medium	Thermo Fisher	Cat#C11995500BT
RPMI 1640 Medium	Thermo Fisher	Cat#C11875500BT
Fetal Bovine Serum, Australia origin	Thermo Fisher	Cat#10099141

EXPERIMENTAL MODEL AND STUDY PARTICIPANT DETAILS

Cell lines

The hepatocellular carcinoma cell line Huh7 and embryonic kidney cell line 293T (HEK293T) were purchased from the Cell Bank of Chinese Academy of Sciences (Shanghai, China). Both cell types were mycoplasma free and were maintained in Dulbecco's modified Eagle's medium (Gibco, Gaithersburg, MD, USA) supplemented with 10% fetal bovine serum (FBS) (Gibco) and 100 U/mL penicillin-streptomycin (Gibco). Cell lines were seeded at a density of 4 × 10^5 cells/mL and passaged at 90% confluence for 20 passages.

Primary cell culture

Human PBMCs were collected from fresh peripheral blood of healthy donors at the Huashan Hospital of Fudan University Shanghai, China. Informed consent was obtained from all subjects involved and the project was approved by the Institutional Review Board of Huashan Hospital, Fudan University (no. 2022–913). Human T lymphocytes were purified using the Pan T cell Isolation Kit (Miltenyi Biotec, Bergisch Gladbach, Germany). T lymphocytes were seeded at a density of 1 × 10^6 cells/mL and cultured in RPMI 1640 medium supplemented with 10% FBS, 2 mM glutamine, 1% MEM non-essential amino acid solution, 10 mM HEPES, and 1 mM sodium pyruvate (All from Gibco).

Animals

NSG mice (NOD.Cg-Prkdc^{scid}Il2rg^{em1Smoc}) were purchased from Shanghai Model Organisms Center, Inc (Shanghai, China). Humanized immune system NSG mice (huHSC-C-NKG-ProF) were constructed in Cyagen Biosciences (Suzhou, China) based on hematopoietic stem cells (HSCs), and mice with comparable levels of immune system humanization (where T cells constitute over 30%, B cells over 10%, and NK cells over 5% of peripheral blood human immune cells) were selected. All animals were housed under pathogen-free, humidity- and temperature-controlled (20–24°C) specific conditions at Fudan University, with free access to water and standard laboratory rodent chow. All animal experiments were approved by the Institutional Animal Care and Use Committee of Fudan University (No. 20210302-124) and conformed to the relevant regulatory standards. In all Huh7 tumor trials, female mice of the same age and similar weight were randomly assigned to different experimental groups. Subcutaneous xenograft tumor model was created in mice and different CAR-T cells were injected for treatment, while un-transduced T cells were used as negative control. The tumor volume in all experiments was calculated as (Length × Width^2) / 2, and a tumor volume > 2000 mm^3 was considered as the experimental endpoint.

METHOD DETAILS

Generation of CAR-T cells

The structure of third-generation GPC3-CAR included a CD28 intracellular domain, 4-1BB intracellular domain, and CD3 zeta intracellular domain, along with a GPC3-specific target scFv derived from the HU9F2 antibody. *Foxp3* was co-expressed with GPC3-CAR via the T2A peptide in GPC3-CAR-Foxp3. Genes encoding GPC3-CAR and GPC3-CAR-Foxp3 were inserted into the lentiviral vector pWPT-GFP (Cat#12255, Addgene) via MluI and SalI cloning sites. To produce lentiviruses, the lentiviral packaging vectors psPAX2 (Cat#12260, Addgene), pMD2.G (Cat#12259, Addgene), and CAR plasmids were transfected into HEK293T cells using polyethylenimine (Polysciences, Warrington, USA). Naive T lymphocytes were activated using anti-CD3 antibody (BioLegend, San Diego, CA, USA) and anti-CD28 antibody (BioLegend) coated wells, and then infected with concentrated lentivirus in RetroNectin (Takara, Shiga, Japan) coated plates to create CAR-T cells. And un-transduced T cells as negative controls underwent the same activation and expansion procedure with CAR-T cells but without viral infection.

Staining and flow cytometry

Cells were washed and blocked with Fc Receptor Blocking Solution (Human TruStain FcX; BioLegend). Next, using certain antibodies and reactive dye, the cells were stained for 30 min at 4°C. After two rounds of washing, the cells were analyzed using a FACSCanto II or FACSCelesta (BD Biosciences, San Jose, CA, USA). Each duplicate consisted of at least 10,000 events, and unstained, untreated cells were also used as controls. Finally, the data were analyzed using FlowJo software (Tree Star, Ashland, Oregon, USA).

ECAR and OCR measurements

The OCR and ECAR were monitored using a Seahorse Bioscience XFe96 Extracellular Flux Analyzer (Seahorse Bioscience, Billerica, MA, USA) in accordance with the manufacturer's recommendations. Different CAR-T cells were purified using flow cytometry sorter (Sony MA900), and 6 x 10^4 CAR-T cells/well were plated on Seahorse XFe96 plates. For measuring OCR, the cells were exposed to 1.5 μM oligomycin, 2.0 μM FCCP, 0.5 μM rotenone, and antimycin A (All from Agilent, Santa Clara, CA, USA) at final concentrations. In contrast, 10 mM D-glucose, 1 mM oligomycin, and 50 mM 2-deoxyglucose (All from Agilent) were injected sequentially to measure the ECAR.

Non-targeted mass spectrometry and analysis

After two washes in PBS, the same number and positive rate of CAR-T$_{Conv}$ and CAR-T$_{Foxp3}$ cells were lysed with an extraction solution (Acetonitrile : methanol : water = 2 : 2 : 1) that contained a mixture of isotopically labeled internal standards. Samples were vortexed for 30 sec, followed by three rounds of freezing and thawing in liquid nitrogen. After sonication in an ice water bath for

10 min, samples were incubated at −40°C for 1 h. Thereafter, samples were centrifuged at 13,000 × *g* for 15 min at 4°C, and the supernatant was collected for LC-MS analysis at Shanghai Baiqu Biomedical Technology Co., Ltd. (Shanghai, China). LC-MS was performed on a Vanquish UHPLC system (Thermo Fisher) with a UPLC BEH Amide column (2.1 mm × 100 mm, 1.7 μm) coupled to a Q Exactive HFX mass spectrometer (Orbitrap MS, Thermo Fisher). The original data were processed using ProteoWizard and peak identification, extraction, alignment, and integration were carried out using an internal tool. An in-house MS2 database was used for metabolite annotation with a cutoff of 0.3. The supervised OPLS-DA method was used to determine the VIP value of the first principal component and to visually distinguish groups and identify metabolites with significantly different levels, which were selected by VIP > 1 and $P < 0.05$. The significantly different metabolites were displayed and pathway enrichment analysis was carried out.

[U-C13]-Glucose and [U-C13]-glutamine metabolism

Metabolic tracer analyses using [U-C^{13}]-glucose and [U-C^{13}]-glutamine as substrates were performed to monitor glycolysis and the TCA cycle. The same number and positive rate of CAR-T_{Conv} and CAR-T_{Foxp3} cells were harvested, washed twice with PBS, and lysed with an extract solution (Acetonitrile : methanol : water = 2 : 2 : 1) after different CAR-T cells were labeled for 6 h in T cell medium supplemented with [U-C^{13}]-glucose (11.11 mM) or [U-C^{13}]-glutamine (2 mM). The supernatants were collected and submitted to the Institute of Metabolism and Integrative Biology (Fudan University, Shanghai, China) for LC-MS analysis. LC-MS analyses were performed using AB SCIEX ExionLC AC high-performance liquid chromatography with an iHILIC-(P) Classic HILIC column (2.1 mm × 150 mm, 5 μm) coupled to an AB SCIEX TripleTOF 6600^{+} mass spectrometer. ProteoWizard was used to process the original data and EI-MAVEN was used to perform peak extraction to gather the response data for each metabolite, and the results were analyzed using R.

RNA extraction and RNA-seq

At the end of animal experiment in Figure 5A, intratumoral CAR-T cells from CAR-T_{Foxp3} and CAR-T_{Conv} groups were purified using flow cytometry sorter (Sony MA900), total RNA was extracted and evaluated using Bioanalyzer. cDNA library was constructed using the Hieff NGS MaxUp II Dual-mode mRNA Library Prep Kit for Illumina (Yeasen, Shanghai, China). After quality control, 150 bp paired-end reads were sequenced on an Illumina NovaSeq 6000 platform (Illumina, San Diego, CA, USA), acquiring approximately 30 million reads. Next, RNA-seq raw data were checked for quality and trimmed using FastQC and Trim Galore, respectively. Hisat2 was used for mapping sequence reads to the human genome (hg38), and Subread was used to count reads. In subsequent differential expression analysis, the limma package was used to filter differentially expressed genes using logFC > 1 and $P < 0.05$ as threshold criteria.

BiFC assay

For BiFC analysis, the complete coding sequence (CDS) or partially deleted *Foxp3* were cloned into pBiFC-VC155 (Cat#22011, Addgene) vector and combined with the C-terminal segment of Venus to form a *Foxp3*-Cvenus fusion protein. Meanwhile, the entire CDS of *Drp1*, *Mfn1*, *Mfn2*, and *Opa1* were inserted into pBiFC-VN173 (Cat#22010, Addgene) vector and combined with the N-terminal fragment of Venus. Subsequently, pBiFC-*Drp1*-VN173, pBiFC-*Mfn1*-VN173, pBiFC-*Mfn2*-VN173, and pBiFC-*Opa1*-VN173 plasmids were respectively transfected into HEK293T cells with pBiFC-*Foxp3*-VC155 plasmid. The fluorescence of the HEK293T cells was observed using fluorescence microscopy and flow cytometry after 72 h.

GST pull-down assays

The *GST-Drp1* fusion protein was created by cloning the full-length *GST* CDS with *Drp1*. The *Foxp3* gene was tagged with a 6*His-tag. Plasmids encoding *GST*, *GST-Drp1*, and *Foxp3*-6*****His were inserted into the PCDH-CMV-EF1a-GFP vector (Cat#CD511B-1, System Biosciences) via EcoRI cloning sites. Proteins were expressed in HEK293T cells via plasmid transfection. After cell lysis, the GST and GST-Drp1 fusion proteins were purified using Glutathione-Magarose Beads (Changzhou Smart-Lifesciences Biotechnology Co., Ltd., Changzhou, China). Whole-cell lysates containing Foxp3-6*His were generated from HEK293T cells transfected with PCDH-CMV-Foxp3-6*His plasmid and incubated with purified GST and GST-Drp1 proteins (∼10 μg) for 2 h at 4°C. After washing, the retained proteins were eluted by boiling and analyzed via western blot using antibodies against GST (Cat#66001-2-Ig, Proteintech) and His-tag (Cat#66005-1-Ig, Proteintech).

Protein interaction analysis

AlphaFold was employed to predict the crystal structures of Foxp3 and Drp1. The protein crystals obtained were subjected to protein preprocessing, regenerating states of the native ligand, H-bond assignment optimization, protein energy minimization, and water removal using Schrödinger software. Next, Foxp3-Drp1 docking was conducted using protein-protein docking module. The number of ligand rotations to the probe was set to 70000 and the maximum number of poses to return was set to 30. The lower the docking score, the stronger the binding stability.

Live cell imaging for cytotoxicity assay

For live cell imaging, different CAR-T cells were purified using flow cytometry sorter (Sony MA900), and Huh7 cells were stained with eFluor™ 670 (Thermo Fisher) and incubated with CAR-T cells at a ratio of 4 : 1. Cytotoxicity was observed using a Nikon Ti2E fluorescence microscope coupled to a Yokogawa W1 Spinning Disk, connected to two SCMOS ZYLA cameras, and equipped with an incubation chamber, Okolab, that controls temperature, CO_2, and humidity. More than 80 Huh7 cells were monitored using this live cell imaging setup. Cytotoxicity was measured based on the total fluorescence intensity calculated using Fiji software (National Institutes of Health, Maryland, USA).

ATAC-seq and data processing

Tregs, CAR-T_{Conv}, and CAR-T_{Foxp3} cells from the same donor were isolated and purified using flow cytometry sorter (Sony MA900). After 3 days of antigen-specific stimulation, CAR-T_{Conv} and CAR-T_{Foxp3} cells were subjected to ATAC-seq analysis using the Illumina NovaSeq 6000 platform (Illumina), along with activated Tregs. FastQC and Trim Galore were used for data quality evaluation and removal of adapter sequences and low-quality bases. SAMtools and Sambamba were used to filter duplicate and multi-mapped reads after Bowtie2 matched the reads to the genome. MACS2 was used for peak calling, and DiffBind was employed to detect differential ATAC-seq peaks. Heatmaps and matrices of the ATAC-seq signals in the TSSs were calculated using the ComputeMatrix tool in DeepTools. ChIPseeker was used to annotate the ATAC-seq peaks and motif analysis based on HOMER.

T cell proliferation suppression assay

Human PBMCs were purchased from Shanghai Oribiotech Biotechnology Co. (Shanghai, China). Treg cells ($CD4^+CD25^+CD127^-$) were isolated from these PBMCs using flow cytometry (Sony MA900) and then expanded with Dynabeads (Thermo Fisher, 11132D). Meanwhile, CAR-T cells and naive T cells were also prepared from these PBMCs of the same donor. After that, naïve T cells were labeled with CFSE and co-cultured with Treg cells or CAR-T cells at a ratio of 2:1 under Dynabeads stimulation for 72 h. Cell proliferation were evaluated by monitoring the dilution of green fluorescent dye CFSE using flow cytometry. The cell proliferation suppression was calculated by Percent suppression = 100 - (Percentage of proliferating cell with Treg or CAR-T cells / Percentage of proliferating cell in group) * 100.

Illustration tool

BioRender is employed for creating the graphical abstract image.

QUANTIFICATION AND STATISTICAL ANALYSIS

Statistical analysis was conducted using GraphPad Prism 8.0 (GraphPad, La Jolla, CA, USA), and all data are indicated as mean ± standard deviation or mean ± standard error of the mean. We employed F-test for comparing variances and two-tailed, unpaired Student's *t*-test to determine the statistical discrepancy for two groups. For three and more groups, one-way and two-way ANOVA was employed. Statistical significance was set at $P < 0.05$ and figure legends include the statistical information for each experiment.